HHS Public Access

Author manuscript

Nat Neurosci. Author manuscript; available in PMC 2022 September 14.

Published in final edited form as:

Nat Neurosci. 2022 April ; 25(4): 504–514. doi:10.1038/s41593-022-01031-7.

Integrating whole-genome sequencing with multi-omic data reveals the impact of structural variants on gene regulation in the human brain

Ricardo A. Vialle[1,2,3,4,5], **Katia de Paiva Lopes**[1,2,3,4,5], **David A. Bennett**[5], **John F. Crary**[1,2,6], **Towfique Raj**[1,2,3,4,*]

[1]Nash Family Department of Neuroscience & Friedman Brain Institute, Icahn School of Medicine at Mount Sinai, New York, NY, USA

[2]Ronald M. Loeb Center for Alzheimer's disease, Icahn School of Medicine at Mount Sinai, New York, NY, USA

[3]Department of Genetics and Genomic Sciences & Icahn Institute for Data Science and Genomic Technology, Icahn School of Medicine at Mount Sinai, New York, NY, USA

[4]Estelle and Daniel Maggin Department of Neurology, Icahn School of Medicine at Mount Sinai, New York, NY, USA

[5]Rush Alzheimer's Disease Center, Rush University Medical Center, Chicago, IL, USA

[6]Department of Pathology, Icahn School of Medicine at Mount Sinai, New York, NY, USA

Abstract

Structural variants (SVs), genomic rearrangements of >50 bp, are an important source of genetic diversity and have been linked to many diseases. However, it remains unclear how they modulate human brain function and disease risk. Here, we report 170,996 SVs discovered using 1,760 short-read whole genomes from aged adults and Alzheimer's disease individuals. By applying quantitative trait locus (SV-xQTL) analyses, we quantified the impact of *cis*-acting SVs on histone modifications, gene expression, splicing, and protein abundance in post-mortem brain tissues. More than 3,200 SVs were associated with at least one molecular phenotype. We found reproducibility of 65–99% SV-eQTLs across cohorts and brain regions. SV associations with mRNA and proteins shared the same direction of effect in more than 87% of SV-gene pairs. Mediation analysis showed ~8% of SV-eQTLs mediated by histone acetylation, and ~11% by splicing. Additionally, associations of SVs with progressive supranuclear palsy identified previously known and novel SVs.

*Correspondence: towfique.raj@mssm.edu.

AUTHOR CONTRIBUTIONS STATEMENT

Conceptualization: TR, RAV; Methodology: TR, RAV; Software: RAV; Formal analysis: RAV, KPL; Resources and data curation: DAB, TR, JFC; Writing - original draft: TR, RAV; Writing - review & editing: TR, DAB, JFC, RAV, KPL; Supervision, project administration, and funding acquisition: TR. All authors read and approved the manuscript.

COMPETING INTERESTS STATEMENT

The authors have declared no competing interest.

Introduction

Structural variants (SVs) are defined as genomic rearrangements ranging from fifty to thousands of base pairs[1–3]. These rearrangements can be classified as unbalanced (e.g., deletions, duplications, and insertions), balanced (e.g., inversions and translocations), or any complex combination of SV classes. SVs are widespread in the human genome and provide an important source of variation during evolution[4,5]. In contrast to single-nucleotide polymorphisms (SNPs) and small indels, SVs can affect a higher fraction of the human genome[6], suggesting that they may have more significant, or at least similar, consequences for phenotypic variation and evolution[4,5]. Current estimates based on short-read sequencing data suggest that a human genome harbors around 7 to 9 thousand SVs[3,7,8] compared to the reference genome, however novel long read sequencing technologies have been showing that these numbers can go up to 27,000 SVs[7,9]. With the increasing number of short-read WGS data produced, the number of genome-wide studies of SVs have been escalating in the past few years, jumping from 2,504 human genomes analyzed in the 1000 Genome Project[1] to 14,891 in GnomAD[3] and 17,795 in NHGRI Centers for Common Disease[2]. Nevertheless, we are still far from a complete and comprehensive population-scale human structural variation catalog.

The contribution of SVs in brain-related disorders and traits such as schizophrenia[10–12], autism spectrum disorder (ASD)[13–15], and cognition[16,17] is notable. However, most studies on the impact of SVs so far have been restricted to non-brain tissues or to mRNA expression level only[18–20]. Large cohort studies, like the GTEx consortium, have already started mapping the impact of common and rare SVs on RNA expression from brain tissues with relatively small sample size[21,22]. Genes expressed in brain tissues have complex features, with one of the highest expression levels and transcriptome complexity[23], the longest introns[24], more alternatively spliced intron clusters[19], along with complex regulatory architecture[25], making them especially vulnerable to SVs of all types. The effects of genetic variants can be modulated at different levels of gene regulation[18–20]. Therefore, identifying the impact of SVs on different molecular phenotypes in the brain is crucial to understanding their functional outcome and role in diseases.

Here, we discovered SVs from whole-genome sequencing (WGS) data of 1,760 individuals from four aging cohort studies: the Religious Orders Study (ROS) and Memory and Aging Project (MAP)[26,27], Mayo Clinic[28], and Mount Sinai Brain Bank (MSBB)[29], all made available to the research community through the Accelerating Medicines Partnership in Alzheimer's Disease (AMP-AD) Knowledge Portal[30]. Then, by integrating multi-omics data sets consisted of histone acetylation (H3K9ac, ChIP-seq), RNA (RNA-seq), and proteomics (TMT-Mass Spectrometry) measured in brain tissues for subsets of the same donors, we mapped the impact of common SVs into multiple molecular phenotypes. We measured the main SVs features associated with each phenotype and the propagation of effects through the regulatory cascade (Figure 1). We also identified pathogenic SVs related to neurodegenerative diseases and the impact of rare SVs on RNA and protein levels.

Results

Structural variation discovery and quality assessment

We analyzed 1,881 human samples with WGS data generated from four cohorts (ROS/MAP, MSBB, and Mayo Clinic). To identify SVs in each group, we run a combination of seven different tools to capture the main classes of variation, including deletions (DEL), duplications (DUP), insertions (INS), inversions (INV), mobile element insertions (MEI), and complex rearrangements (CPX). These variants were further merged and genotyped at the group level (Supplementary Figure S1). After pre- and post-discovery quality control (QC; Supplementary Table S1, Supplementary Figure S2), a total of 170,966 'high-confidence' SVs were identified in 1,760 samples that were used for all subsequent downstream analyses (Figure 2a). As expected, more SVs were detected in the ROS/MAP cohorts due to the larger sample size (n=1,106). More SVs were detected in MSBB compared to Mayo, due to ancestry differences[1,3] as the Mayo data is composed of European ancestry individuals only, while MSBB has more diverse populations, including individuals of African and Admixed American ancestry (Supplementary Figure S3). Most SVs were small (median size of 280 bp), comprised by mostly deletions and insertions, with a decreasing frequency as the variants increased in size and with a high number of *Alu*, SVA, and LINE1 mobile element insertions identified (Figure 2b).

To assess the quality of SVs discovered, we first measured the reproducibility of our calls compared to other large datasets, including dbVar[31], Centers for Common Disease Genomics (CCDG)[2], Database of Genomic Variants (DGV)[32], Deciphering Developmental Disorders (DDD)[33], GnomAD-SV[3], and 1000 Genomes Project[1]. We found about 30% of novel SVs and, as expected, the highest proportion of these SVs were discovered as singletons (Figure 2c). Overall, 89% of deletions and 92% of insertions were reproducible across AMP-AD cohorts, while around 56% of duplications and inversions found in ROS/MAP were also identified in Mayo or MSBB. Comparing external cohorts, we observed considerable reproducibility for deletions, with 62% of SVs discovered in ROS/MAP also being mapped in gnomAD and 44% in the 1000 Genomes Project, followed by insertions (55% and 34%, respectively). Duplications and inversions were less reproducible (Supplementary Figure S4). Further, allele frequency comparisons of SVs in common with the 1000 Genomes Project and gnomAD-SV showed high overall reproducibility with R^2 equal to 0.75 and 0.71, respectively (Supplementary Figure S5). We also observed that about 75% of SVs were in Hardy–Weinberg equilibrium depending on the study (Supplementary Figure S6). In addition, we generated long-read WGS with PacBio for two ROS/MAP samples. We performed *in silico* confirmation of 3,581 SVs identified with short-reads and accessed a confirmation of 84.3% of them (Figure 2d, Supplementary Figure S7). Together, these analyses provided sufficient evidence for the quality of the SVs discovered across all samples.

In accordance with previous studies[1,3,21,34,35], a substantial proportion of SVs detected were rare (71%, minor allele frequency (MAF) < 0.05). More than 30% of SVs were observed in only one individual (Extended Data Fig. 1a). Additionally, by overlapping SVs with genomic annotations, we observed that singletons were more likely to occur

in coding and regulatory regions compared to all other SVs (Extended Data Fig. 1b). Moreover, constrained genes, such as morbid genes, loss-of-function (LoF) intolerant, and haploinsufficient genes, were more likely to be disrupted by singletons and ultra-rare SVs, reflecting the effects of purifying selection (Extended Data Fig. 1c–e). These analyses demonstrate that the structural variants found here conform with principles of population genetics and highlight the importance of large sample sizes to improve the characterization of rare and pathogenic variants.

Effects of SVs on gene expression

We performed associations of common SVs with gene expression in *cis* for the available brain regions (Figure 3a). The number of associations was highly correlated with the sample size (Pearson's r 0.98, P-value 5×10^{-5}). DELs and SVA transposons were more likely to be associated with changes in expression, while INS were less likely (Figure 3b). Pseudogenes, long non-coding RNAs (lncRNAs), and TEC (To be Experimentally Confirmed) were significantly more likely to be associated with SVs, and their overall effect sizes were higher compared to protein-coding genes (Figure 3c–d). Such differences support evidence that less constrained genes are more likely to be eGenes in agreement with results previously observed for SV and SNV eQTLs[35,36]. The direction of effects (β) of SV-eQTLs was mostly distributed in both directions, except when the SVs were overlapping the exons (3.6%) (Figure 3e), in these cases, the observed differences could be also attributed to technical artifacts in the quantification (e.g., duplicated exons resulting in increased expression).

Comparison between different brain regions showed 98% of shared SV-eQTL with the same direction of effect (β) (Supplementary Figure S8). The reproducibility of SV-eQTL across studies, as measured by Storey's π1 and mashR[37], showed substantial sharing of effects on brain gene expression (Extended Data Fig. 2). The highest reproducibility was observed within regions from the same studies, as a consequence of repeated donors (77,1% and 86.7% of donors from Mayo Clinic and MSBB, respectively, had RNA-seq for more than one brain region). However, regional effects were also observed when comparing different studies, for example, TCX and DLPFC shared more effects than DLPFC and CBE (0.81 and 0.74, respectively) (Figure 3f), suggesting some degree of regional specificity.

To measure brain specific effects, we also mapped SV-eQTL using RNA-seq from $CD14^{+}CD16^{-}$ isolated monocytes generated from ROS/MAP samples (n=177, with 41 samples overlapping the DLPFC RNA-seq). We observed a replication of 0.72 (Storey's π1) in DLPFC. Majority of effects were concordant (Pearson's $r = 0.6$) but considerably lower than between brain regions (Extended Data Fig. 3). We also compared the SV-eQTLs from AMP-AD with other tissues from GTEx[21,22]. Due to differences in SV discovery pipelines and RNA-seq tissues, cross mapping between the two datasets was limited. A total of 210 SV-eQTL could be mapped significantly associated in both datasets. (Supplementary Figure S9).

In order to infer possible causality of SVs in each locus we performed joint eQTL with SV and SNPs for the ROS/MAP cohort finding a total of 7,787 eQTL where 95 (1.2%) had SVs as lead variant. We also performed fine-mapping using CAVIAR[38] to access the causality probability of each variant tested while accounting for LD structure as previously

performed[21]. As result, 86/2519 (3.41%) showed CAVIAR probabilities higher or equal than SNPs (Figure 3g). While the true causal variant at these loci is unknown, these data suggest that a substantial number of eQTLs that can be identified using SNVs may be explained by SVs. Among these, we can identify cases where SNPs are found in high LD with the lead SV highlighting that possible causal haplotype association, as for example for the gene *MPC2* (Figure 3h), in a locus previously associated with schizophrenia[39]. While in some cases, the effects seem to be caused by SVs with no detectable SNPs in high LD such as for the gene *FAM66C* (Figure 3i) where a 29 kb duplication is associated with expression changes, suggesting an example of eQTL only found through SV mapping. Although, we expect that these number are underestimated due to typically higher genotyping errors for SVs and limited SV discovery using short-reads compared to SNPs and small indels[21].

Mapping of SVs that affect the gene-regulatory cascade

We mapped associations of 25,421 SVs with MAF ≥ 0.01 in the ROS/MAP cohorts to four different molecular phenotypes in the DLPFC. These molecular phenotypes were measured for a partially overlapping set of samples (Supplementary Figure S10) and included gene expression for 15,582 genes (n=456), 110,092 splicing junctions proportions measured by "percent spliced in" values (PSI) (n=505), histone acetylation (H3K9ac) peaks (n=571), and proteomic data for 7,960 proteins (n=272). We refer to these analyses as SV-xQTL, in which we map differences in measurements of each molecular phenotype associated with specific SV's (Figure 1). Therefore, each SV-xQTL is an SV-phenotype pair (i.e., SV-eQTL, SV-sQTL, SV-haQTL, or SV-pQTL). All phenotype measurements were adjusted prior to associations to account for known (e.g., sex and ancestry principal components) and unknown covariates, and the allele alternative to the genome of reference was considered as effect allele. This identified 3,191 SV-eQTL, 2,866 SV-sQTL, 399 SV-pQTL, and 1,454 SV-haQTL (FDR < 0.05) (Figure 4a, Extended Data Fig. 4).

The majority of SVs associated with one or more molecular traits were found near gene bodies. For instance, more than 87% of SVs associated with H3K9ac peaks (haSVs) had at least one breakpoint within 500 kb of the closest gene, while more than 93% of splicing associated SVs (sSV) were found within 50 kb of the respective gene bodies (Supplementary Figure S11). Additionally, the direction of effect for the associations (β) were usually distributed in both directions for SV-xQTLs, independently of SV class, reflecting possibly complex enhancing and repressing regulatory effects or loci with SVs in linkage disequilibrium (LD) with the true causal variants. The biological assumption that gene dosage effects (e.g. gene duplications) are likely to cause increased total level of expression usually relies on the duplication of regulatory regions as well, these duplications tend to relax the level of selection on these genes and subsequently result in "subfunctionalization"[40]. As has been observed by other SV studies[21,41], since gene-level expression values are normalized to the reference transcript length[42], partial exonic duplications altering the transcript length are expected to modulate expression values even if the absolute number of transcripts remained stable. This could be observed when the SVs overlapped the phenotypes (e.g., exonic region or histone peak) where the effects of deletions and MEIs were mostly negative, while duplications were mostly positive (Extended Data Fig. 5).

By measuring associations for each SV class separately, we observed that specific classes were more likely to be associated than others in each phenotype. Deletions in particular showed enrichment of associations compared to all classes together, while insertions were depleted. *Alu* elements, despite being known to promote alternative splicing[43,44], were enriched in eQTLs and pQTLs but not in the other two traits, while SVA elements were enriched in eQTL, pQTL and sQTLs (Figure 4b). SVAs are considerably less frequent than other transposable elements and their effects on splicing, expression, and protein could be due to SVAs acting as novel promoters[45] or exon-trapping[46]. Additionally, SV-xQTLs were enriched in relevant functional annotations similarly across all molecular phenotypes (Figure 4c). However, some specific phenotypes showed stronger enrichment than others. For instance, haSVs were strongly enriched in regulatory regions, such as promoters, enhancers, and CTCF sites.

We identified 667 SV-gene pairs associated with at least two phenotypes with highly concordant effects. The correlation of effect sizes between eQTLs and pQTLs was 0.71 (Pearson correlation) and between pQTLs and haQTLs 0.77, while eQTLs and haQTLs showed slightly weaker correlation (Pearson correlation = 0.59) (Figure 4d, Supplementary Figure S12). In addition, 241 SVs were found affecting at least three phenotypes, and 25 SVs affecting all four measured phenotypes in several loci such as *HLA, GSTM, GSTT, RBM, BPHL, VARS2, CAB39L, RLBP1, GCSH, DECR2,* and *PHYHD1*. No statistically significant differences were found between these SV affecting all phenotypes compared to rest (SVs associated with one to three phenotypes) in terms of length (t-test, *P*-value = 0.78) or SV class (chi-squared test, *P*-value = 0.47). Although, effect sizes of SVs affecting all four phenotypes had significant slightly lower absolute values compared to the rest of SVs (t-test, *P*-value = 0.008). Moreover, more than 62% of SVs associated with proteins (pSVs) were also associated with differential RNA expression (Figure 4e). While the majority (87%) of the SV-pQTLs and SV-eQTLs were concordant (Figure 4d), few had discordant effects; for example, in the gene *UROS*, a 411 bp duplication located in the promoter region of the gene was associated with lower RNA expression, but higher protein expression, suggesting some complex regulatory mechanism (Figure 4f). Additionally, 25.5% and 23.7% of pSVs were also associated with histone markers and splicing, respectively, suggesting distinct mechanisms for gene regulation, while 28% were found associated with proteins only (Figure 4e). By contrast, 50% and 47% of splicing and histone associated SVs were also SV-eQTLs, respectively (Supplementary Figure S13).

To get a better understanding of how each SV-xQTL layer relates to each other, we also performed mediation analysis using *bmediatR*[47]. Three causal models were tested: complete mediation, partial mediation, and co-local (SV independently affects two phenotypes) (Figure 5a). We considered either RNA or proteins genes found associated at FDR 5% (i.e., 2,518 eGenes and 329 pGenes) as outcome and the other phenotypes as mediators. Samples were matched in each pairwise comparison. H3K9ac and splicing mediation effects on proteins were found less prominent than the effects on RNA, with a lower proportion of pQTLs explained through complete or partial mediation. For instance, considering RNA levels as outcome, 7.94% of eQTLs were mediated (complete and partial) by H3K9ac, while 11.72% were mediated via splicing (Figure 5b), while for proteins as outcome, only 2.43% and 4.86% were mediated though these mechanisms respectively (Figure 5b). This

difference might be caused by the smaller sample size with proteomics data (approximately 4-fold difference, compared to RNA). Overall, a large proportion of SV-xQTLs were independent (co-local effects), explaining ~8–18% of eGenes and ~10–14% of pGenes. reflecting the weak correlation between phenotypes. Effects where complete mediation was observed were rarer, but still observable, like the mediation of *RP11–33B1* SV-eQTL by SV-haQTL (Figure 5d). Additionally, similarly as observed for SNP-eQTLs and -pQTLs[48], a considerable proportion of proteins were mediated by RNA levels (14.29%, complete and partial), while around 13% showed independent associations. We also measured the mediation of the genetic effects on mRNA by protein and identified a few cases (3.22%) where the effects of SV-eQTL could be explained by SV-pQTLs. Around 30% of SV-eQTL were completely or partially mediated by different SV-pQTL genes. For example, a 3.7 kb deletion associated with *ACOT11* SV-pQTL seems to mediate the SV-eQTL of *MROH7* (complete mediation posterior probability = 0.59) just downstream (Extended Data Fig. 6).

Effects of rare SVs

In contrast to common variants which are widespread in a population and have been subjected to a long process of natural selection, rare variants are usually much more recent and their impact on phenotypes more deleterious[21,49]. Due to their low frequencies, the impact of rare variants is usually measured indirectly by looking for enrichments within outliers, instead of performing standard association tests[49,50]. To assess the impact of rare SVs in gene expression first mapped gene-sample expression outliers for RNA and protein levels measured in ROS/MAP and we assessed the enrichment of rare variant carriers nearby those genes.

We identified 1,551 and 1,747 gene-sample outlier pairs for RNA expression and protein levels, respectively. A higher proportion of outliers was observed in proteins compared to RNA when considering samples and genes measured in common (112 samples and 7,546 genes) (Figure 6a). Additionally, only 43 (5%) gene-sample pairs were replicated between both phenotypes, reflecting the modest correlation (Spearman's $\rho = 0.38$) observed between average RNA expression and protein levels (Supplementary Figure S14).

Next, we measured the enrichment of rare SVs (MAF < 1%) overlapping gene bodies of outliers (for RNAs and proteins, separately). We found significant enrichment of SV classes in these conditions, especially deletions and duplications, with stronger enrichments in RNA compared to proteins (Figure 6b). This could be due to smaller sample sizes and the smaller number of genes tested. The direction of differential expression correlated with the expected dosage alteration effect (Figure 6c), but we still observed many cases in opposite directions suggesting more complex regulatory effects (Figure 6d). Six gene-sample outliers with overlapping rare SVs were found with effects on RNA and protein levels, including a homozygous rare 103 kb duplication causing overexpression of *C19orf12* and a homozygous 136 bp deletion causing underexpression of *TLN2* in the respective variant carriers (Figure 6e).

Characterizing pathogenic SVs in neurodegenerative diseases

Since SVs are not usually included in GWAS, their association with neurodegenerative diseases and complex traits has been overlooked. We investigated SVs tagging GWAS variants, by measuring the LD between SVs with SNVs in ROS/MAP and comparing them with EBI GWAS Catalog variants. We found 802 common SVs by proxy associated (R^2>0.8 between the SV and the SNPs) with 534 traits (GWAS *P*-value < 5×10^{-8}). Among these SVs, 344 SVs were associated to some molecular phenotype in the brain and 47 SVs were found in LD with brain related GWAS, including schizophrenia, autism, bipolar disorder, multiple sclerosis, corticobasal degeneration (CBD) and progressive supranuclear palsy (PSP). These associations might help the understanding of the genetic mechanism involved in these risk loci. For example, we mapped a 129 bp deletion upstream of *SRR,* a gene involved in glutamatergic neurotransmission and synaptic plasticity, which is in LD with GWAS variants for schizophrenia (rs8070345, $R^2 = 0.94$)[51]. This deletion was also found associated with a H3K9ac peak, and with reduced expression of *SRR* at RNA and protein levels (Extended Data Fig. 7). Another 5 kb deletion in chromosome 3, was also in LD with another schizophrenia GWAS SNP (rs66691851, $R^2 = 0.95$). The deletion was an SV-eQTL the gene *PCCB* and also showed association with a H3K9ac peak in the promoter region of *STAG1*, possibly distally linked by a CTCF disruption (Extended Data Fig. 8). We also identified an 82 bp insertion in LD with an Alzheimer's disease loci (rs73045691, $R^2 = 0.80$), with associations with changes in expression of *ACOC1* and splicing of *APOC2* (Extended Data Fig. 9).

In addition, we also performed one of the first genome-wide SV associations with Alzheimer's disease (AD) and progressive supranuclear palsy (PSP). By combining all SVs across AMP-AD cohorts, we generated a combined call set with 29,177 SVs (22,007 with MAF > 1%) in 1,757 samples. In AD (539 cases, and 368 controls) no SVs were associated with the disease, however, some suggestive hits were observed (Supplementary Figure S15). By contrast, for PSP (83 cases, 368 controls), identified four SVs after Bonferroni correction (Figure 7a). These variant alleles were highly correlated with each other and tagged known distinct haplotypes at the 17q21.31 locus defined by an almost 1 Mb inversion (Figure 7b). These haplotypes were previously reported to be associated with PSP and Parkinson's disease, with the inverted haplotype being protective in both diseases (Odds ratio of 0.2 and 0.8 respectively)[52–54]. In addition, many of these SVs showed associations with changes in gene expression and other molecular phenotypes (Figure 7c). Of the associations replicated in at least one brain region across studies, we found higher expression of *DND1P1*, *KANSL1*, *ARL17A*, *LRRC37A* in the inverted haplotypes (Figure 7c) and differences in *MAPT* splicing junctions and several histone acetylation markers could be detected in ROS/MAP (Figure 7c). Recently a mechanism involving neuron-specific changes in chromatin accessibility and 3D interaction has been proposed[55]. However, additional studies are needed to demonstrate these effects on regulatory interactions.

Discussion

By integrating whole-genome sequencing with multi-omics data, we measured the impact of structural variation in the human brain. We reported over 170 thousand SVs constructed

using 1,760 short-read whole genomes from aging cohorts. We performed SV-xQTL analyses to quantify the impact of cis-acting SVs on H3K9ac histone modification, mRNA expression, mRNA splicing, and protein abundance. We showed that SV-eQTL effects are mostly shared across different brain regions and that many effects can be mediated through the regulatory cascade. We also identified pathogenic SVs related to neurodegenerative diseases and the impact of rare SVs on RNA and protein levels.

Detecting SVs accurately is a challenging task and limitations due to sample size and sequencing read length are the main challenges to the field[56]. Our results showed improved sensitivity of SV detection compared to single algorithmic approaches (Extended Data Fig. 10) as well as high orthogonal discovery confirmation on selected samples. Given the limitations of short-read data, SV discovery sensitivity is still underestimated for some SV classes, such as large insertions and complex configurations. However, we not only observed high reproducibility of SVs compared to independent large SV cohort studies and databases, but we also identified novel variants emphasizing the improvement of discovering SVs from novel samples and diverse populations.

Most studies on the impact of SVs have been restricted to the level of mRNA expression[1,21,35,41]. However, mRNA is not the only determinant of cellular functions[57]. Previous studies based on SNVs and small indels found that QTL effects can be modulated at different levels of gene regulation[18–20]. Here, we identified properties of SVs affecting different molecular phenotypes, identified regions and genes more susceptible to associations, and correlated their effects on phenotypes in terms of both common and rare SVs. Our SV-xQTLs results recapitulated similar trends from SNVs. For example, the majority of SVs associated with proteins were also SV-eQTLs, similar to what has been observed with SNV QTLs[18], and over 14% of SV-pQTLs showed evidence of mediation through SV-eQTLs. Although sQTLs and eQTLs tend to have independent lead variants in SNVs[19], for SVs we observed that half of splicing SVs were also expression SVs, with a modest negative correlation between effect sizes. Additionally, many effects seemed to be specific to a phenotype with about 28% in SVs associated at protein level only which is 3-fold more than SNVs[18]. These data suggest that distinct mechanisms are involved in translating genotype to phenotype.

Interestingly, distinct SV classes seem to have different functional impacts on gene regulation. Transposable elements were shown to contribute to almost half of open chromatin regions[58] and affect more than three fourths of promoter regions, with particular enrichment of short interspersed nuclear elements (SINE) (e.g., *Alu* elements)[59]. Here we found that *Alu* and SVA (composed of SINE-VNTR-Alu) elements are more likely to affect gene and protein expression compared to other SV classes. SVA elements in particular are more evolutionarily recent than other TEs and many are human-specific[45,60–62]. Their importance for gene expression were described both *in vitro* and *in vivo*[63–66]. Our results support an important role for SVA in gene regulation, with more than 2-fold greater chance of being associated with either gene expression, splicing, and protein levels (Figure 4b).

While most of the common SV-xQTL associations can be confounded by LD with actual causal SNVs[21], rare SVs impacting expression outliers at RNA and protein levels can

provide a better sense of SV causality[50]. Here we expand previous analysis[21,49] mapping expression outlier genes in individuals carrying rare SVs, not only at mRNA but also at protein levels. We found more than 10% of mRNA outliers being overlapped by a rare SV, with clear causal resulting effect (e.g., deletions causing reduced expression while duplications causing increased expression). Interestingly, rare and common *Alu* elements seemed to have opposite effects on mRNA expression. Rare *Alu* insertions were found only in overexpression outliers (Figure 6d), while common *Alu* carriers were mostly associated with decreased expression (Figure 3e). Additionally, effects of rare SVs seem to be attenuated at protein levels, given a lower proportion of outliers explained by nearby SVs and an even lower proportion of effects shared between RNA and proteins, reflecting low correlation observed in the expression levels (Supplementary Figure S14).

It is also important to highlight the limitations in our study. Differences in SV discovery and genotyping methods might introduce specific biases[67]. Therefore, some SVs may show discrepancies in terms of allele frequencies compared to other studies[1,3]. Additionally, differences in sample size, and as consequence discovery power, among the different phenotypes might create bias toward specific relationships depending on how results are interpreted. For example, the sample size for proteomics (n=272) is roughly half the size of H3K9ac (n=571) and RNA-seq (n=456) data. Although it is reasonable to expect that effect size observed with smaller sample sizes to be reproduced in large sample sizes, the number of SV-xQTLs are not directly comparable. Particularly for the mediation analysis, the sample sizes were matched according to the outcome analyzed, therefore sample size is less of an issue. However, for other analysis in the manuscript we approached the differences in sample size by either comparing *P*-value distributions (using Storey's $\pi 1$) or by meta-analysis (using MASH[37]) instead of using significance thresholds.

In summary, our study expands the catalog of high-quality SVs by measuring their impact through a gene regulatory cascade and provide a powerful resource for understanding mechanisms underlying neurological diseases.

METHODS

Study cohorts

In our analysis, we included samples from four cohorts (ROS/MAP[26,27], MSBB[29], and Mayo Clinic[28]) from the Accelerating Medicines Partnership in Alzheimer's Disease (AMP-AD) consortium[30]. These aging cohorts provide an extensive collection of multi-omics data, that includes deep whole-genome sequencing (WGS) from 1,860 subjects and allow us to identify SVs and characterize their functional impact. Each cohort is briefly described in the Supplementary Methods). The original study data was obtained from each subject and the ROS/MAP were approved by an Institutional Review Board (IRB) of Rush University Medical Center. WGS data were processed with an NYGC automated pipeline. Paired-end 150 bp reads were aligned to the GRCh37 human reference using the Burrows-Wheeler Aligner (BWA-MEM v0.7.8) and processed using the GATK best-practices workflow (more details in the Supplementary Methods).

SV discovery pipeline

Structural variation discovery was performed running a combination of seven different tools per sample: *Delly* v0.7.9[68], *LUMPY* v0.2.13[69], *Manta* v1.5.0[70], *BreakDancer* v1.4.5[71], *CNVnator* v0.3.3[72], *BreakSeq* v2.2[73], and *MELT* v2.1.5[74]. These variants were further merged at the individual level using SURVIVOR[75] and genotyped at the cohort level using smoove. After pre- and post-discovery quality control were identified 46,197 SVs in Mayo Clinic (349 samples), 52,451 SVs in MSBB (305 samples), and 72,348 SVs in ROS/MAP (1,106 samples), totaling 170,966 across 1,760 samples. Detailed description of the pipeline and quality control is described in the Supplementary Methods.

Linkage disequilibrium between SVs and SNPs

Small variant calls from ROS/MAP samples were generated according to methods described elsewhere [26]. Briefly, WGS reads were aligned to the GRCh37 reference genome using BWA-mem and variant calling was performed using GATK pipeline. Resulting VCF files were obtained from Synapse portal (syn11707419) and then variants were filtered using PLINK v2 keeping biallelic SNPs with call rate > 95%, minor allele frequency (MAF) > 1%, Hardy-Weinberg equilibrium (HWE) P-value > 1 × 10–6, and sample call rate > 95%. Additionally, variants were annotated with dbSNP (All_20180423.vcf.gz). Resulting VCFs files where then merged with SV calls resulting in a joint call set with 8,566,510 SNPs and 72,348 SVs. LD was calculated in terms of R-squared for all SVs using PLINK v2 and considering a window of 5 Mb. As result, 9,876 SVs had a tag SNPs with $r^2 > 0.8$.

Reproducibility of SVs in other large cohort studies

SVs discovered in the AMP-AD cohorts were compared with other large cohort studies and datasets in order to identify novel variants. SV annotations were obtained from *AnnotSV* v2.1[76] and included dbVar[31], the National Human Genome Research Institute (NHGRI) Centers for Common Disease Genomics (CCDG)[2], Database of Genomic Variants (DGV)[32], Deciphering Developmental Disorders (DDD)[33], GnomAD-SV[3], and 1000 Genomes Project SVs[1]. SVs were considered replicated in other datasets if their coordinates had a reciprocal overlap of 0.7 irrespectively of the SV class.

Allele frequency comparison with 1000 Genomes Project and gnomAD-SV

Correlation of minor allele frequencies (MAFs) between SVs discovered in gnomAD-SV and 1000 Genomes Project phase III (1KGP) were compared to ROS/MAP MAFs. Only European (EUR) MAFs from gnomAD and 1KGP were used for comparison. SVs in common were first identified using *bedtools* "intersect" requiring at least 50% reciprocal overlap with no requirement of matching SV classes. Then, coefficients of determination (R^2) were assessed with a linear regression between MAFs for SVs mapped in both studies being compared. Using ROS/MAP as reference, 20,414 (28%) and 15,108 (21%) were found in common with gnomAD and 1KGP respectively. Comparing European MAF between these sets, resulted in correlations of 0.71 for gnomAD and 0.75 for 1KGP. (Supplementary Figure S5).

Hardy-Weinberg equilibrium comparison

SV genotype distributions were evaluated under the null expectations set by the Hardy-Weinberg equilibrium (HWE; $1 = p^2 + 2pq + q^2$). Using tabulated genotype distributions per cohort as input, we measured deviations from HWE using a chi-square goodness-of-fit test with one degree of freedom and their *P*-values using the "HardyWeinberg" package in R[77]. SVs were considered in violation of HWE if its *P*-value was significant after Bonferroni correction for the number of SVs tested per population (Supplementary Figure S6). We did not remove SVs failing the test, but instead we provide the *P*-values as part of the summary statistics tables on GitHub.

SV long-read validation

Two samples from ROS/MAP cohorts were selected for long-read sequencing validation (more details in the Supplementary Methods). DNA samples extracted from DLPFC tissues were then used for continuous long-read (CLR) sequencing using PacBio Sequel II platform. Both samples were multiplexed sequenced in a single SMRT Cell 8M Tray, resulting in an average 10x coverage per sample and average 14 kb read length (Supplementary Table S2). Under such coverage we expect over 80% of F1-score (96.19% precision / 69.12% recall) on GiaB benchmarking[78]. Raw PacBio BAM files were then aligned to the GRCh37 reference genome using *minimap2*[79] and SVs were called using SVIM[80] with default parameters (Supplementary Figure S16). BAM files were used to validate SVs found using the orthogonal short-read data using *VaPoR*, a software that performs comparative local realignments of long-reads to a synthetically modified reference sequence[81].

Therefore, SVs identified in the main SV discovery step with short-reads and positively genotyped in each sample were selected and filtered to maximize *VaPoR* sensitivity. We restricted the analysis for SVs with no overlapping breakpoints to simple repeats, segmental duplications, centromeres, regions subject to somatic V(D)J recombinations, and regions with low mappability in the PacBio data (<10x coverage). SV classes were evaluated separately by deletions, duplications, and insertions. For inversions, since our calls were not completely resolved and could represent also other sorts of complex conformations, we measured their support either as simple inversions (INV) or any combination of deletions, duplications, and inversions (e.g DEL_INV, DUP_INV, DEL_DUP_INV). SVs with a proportion of reads supporting the predicted structure versus all reads assessed higher than zero (i.e., VaPoR_gs > 0) or SVs with genotype proposed by *VaPoR* other than homozygous to the reference (i.e., 0/0) were considered supported in the long-read data. Supporting rates for each sample were then measured as the number of supported SVs divided by the total number of tested SVs (Figure 2d).

RNA-seq processing and SV-eQTL mapping

Given that originally each cohort had different RNA-seq processing pipelines, we took advantage of the RNA-seq Harmonization Study (rnaSeqReprocessing) data (Synapse:syn9702085), which reprocessed all the data in a harmonized workflow (more details in the Supplementary Methods). We mapped SV-eQTL to scan for significant associations between common structural variants and gene expression. We tested SVs with MAF ≥ 0.01 using a modified version from *FastQTL*[21,82] to address the span of breakpoints

within a 1 Mb window from each gene TSS. All association tests were performed considering the allele alternative to the reference genome as the effect allele. A permutation test was applied to select the lead SV per gene and *P*-values were adjusted for multiple testing using Benjamini-Hochberg (FDR). Associations were performed separately for each SV class, meaning that multiple lead-SVs (from different classes) could be associated with each phenotype. A significance threshold of FDR 5% was used in most of the analysis. The total number of significant associations at other thresholds can be found at Supplementary Figure S17.

SV-haQTL mapping

ChIP-seq experiments and data processing for H3K9ac acetylation markers were previously performed on 712 samples (699 after QC) Epigenetics (ChIP Seq) - syn4896408 (synapse.org)[83]. Detailed description of the data processing can be found in the Supplementary Methods. For SV-haQTL analysis, we used residualized values obtained from 571 samples with WGS after regressing out “Sex”, “gel_batch”, “AgeAtDeath” and the first 3 principal components of the genotype matrix to account for the effect of ancestry plus the first 10 principal components of the phenotype matrix to account for the effect of known and hidden factors (Supplementary Figure S18). We tested SVs with MAF ≥ 0.01 and within 1 Mb of each peak. A permutation test was applied to select the lead SV per peak. Finally, *P*-values were adjusted for multiple testing using Benjamini-Hochberg (FDR). Associations were performed separately for each SV class, meaning that multiple lead-SVs (from different classes) could be associated with each phenotype. A significance threshold of FDR 5% was used in most of the analysis. The total number of significant associations at other thresholds can be found at Supplementary Figure S17.

SV-pQTL mapping

Tandem Mass Tag (TMT) isobaric labeling data were previously generated for 292 individuals[84,85]. For SV-pQTL analysis, we used residualized values for 7,960 protein obtained from 272 samples with WGS after regressing “PMI”, “Sex”, “AgeAtDeath”, three first ancestry PCs, and the first 10 principal components of the phenotype matrix (Supplementary Figure S19). We tested SVs with MAF ≥ 0.01 and within 1 Mb of each protein. A permutation test was applied to select the lead SV per protein. Finally, *P*-values were adjusted for multiple testing using Benjamini-Hochberg (FDR). Associations were performed separately for each SV class, meaning that multiple lead-SVs (from different classes) could be associated with each phenotype. A significance threshold of FDR 5% was used in most of the analysis. The total number of significant associations at other thresholds can be found at Supplementary Figure S17.

SV-sQTL mapping

Splicing junction proportions, measured as percent spliced in (PSI), were measured previously[86] (more details in the Supplementary Methods and Supplementary Figure S20). A total of 505 samples with WGS data were used in the association analysis using a modified version from *FastQTL*[21,82] to address when the span or breakpoint of deletions, duplications, inversions, or insertions felt within the *cis* window a gene TSS. Genotyping information of SVs with MAF ≥ 0.01 and within 100 kb of each intron junction were

tested, and a permutation test was applied to select the top SV per junction. Finally, *P*-values were adjusted for multiple testing using Benjamini-Hochberg (FDR). Associations were performed separately for each SV class, meaning that multiple lead-SVs (from different classes) could be associated with each phenotype. A significance threshold of FDR 5% was used in most of the analysis. The total number of significant associations at other thresholds can be found at Supplementary Figure S17.

SV-eQTL sharing

To estimate and compared the SV-eQTL sharing across different brain regions and cohorts, we performed a Multivariate Adaptive Shrinkage (MASH) through the R package *mashR* [37]. Following the pipeline applied by GTEx Consortium [37], the nominal statistics associations from *FastQTL* (*P*-values, betas, and standard errors) for each brain region (DLPFC, TCX, CBE, BM10, BM22, BM36 and BM44) were used as input. The pipeline then: i) selects the strongest associations based on a sparse factorization matrix of z-scores; ii) computes covariance matrices priors using the Extreme Deconvolution method; iii) computes the maximum-likelihood estimates of the weights; and iv) calculates posterior statistics using the fitted MASH models. *mashR* then returns tables with posterior means and local false sign rate (*lfsr*), as a measure of false discovery rate. To measure sharing, we considered the top SV-eQTLs that were significant (*lfsr* < 0.05) in at least one of the two tissues (n = 1,081–1,364 gene-SV pairs, depending on pair of tissues compared). The proportion of sharing by sign was considered if effect estimates had the same direction. While the proportion of sharing in magnitude was measured based on effect estimates that are in the same direction and within a factor of 2 in size.

SV-eQTL fine-mapping

In order to predict the probability of a variant to be causal for a particular eGene, we first mapped SV-eQTL using the joint variant call set (including SVs and SNPs). The VCF was first subsampled to match the 456 samples with DLPFC RNA-seq, and variants were filtered by MAF ≥ 1%, resulting in 7,861,048 SNPs and 23,700 SVs. *Cis*-eQTL mapping was performed using *FastQTL* with 1 Mb window from each gene TSS. A total of 7,787 joint-eQTLs were identified with FDR < 5%. Z-scores were then computed for each variant-gene pair using the linear regression slopes and their nominal *P*-values, which were then used as input for *CAVIAR* [38]. *CAVIAR* is a fine-mapping tool that assesses summary statistics while accounting for the LD across an associated locus to rank the causal probability of each variant in a region. For each gene we ran *CAVIAR* with a causal set size of 1 and using the Z-scores and pairwise LD matrices were obtained for the top 100 variants including the best SV associated (if not among the 100 variants). Posterior probabilities were then obtained as a measure of causality for each variant. 95 of 7,787 eQTLs (1.2%) had an SV with higher *CAVIAR* posterior compared to SNPs.

SV-eQTL mapping in monocytes

CD14+CD16- isolated monocytes RNA-seq data from ROS/MAP samples were obtained from Synapse portal (syn22024496). Sequencing reads were processed following the GTEx eQTL pipeline[87] (more details in the Supplementary Methods) SV-eQTL mapping was performed for 177 ROS/MAP samples with post-QC SV calls (41 donors overlapped with

DLPFC RNA-seq samples). Associations were measured using the modified version from *FastQTL*[17,83] considering the span of breakpoints within a 1 Mb window from each gene TSS. A total of 12,929 genes and 17,347 SVs with MAF ≥ 5% were evaluated. After a permutation test was applied to select the lead SV per gene and *P*-values were adjusted for multiple testing using Benjamini-Hochberg (FDR), a total of 208 SV-eQTL were found in monocytes.

SV-xQTL mediation analysis

We performed mediation analysis using *bmediatR*[47]. The method uses a Bayesian based model selection approach. Three causal models are defined: complete mediation, partial mediation, and co-local (whereas an SV is independently affecting two phenotypes). Mediation was performed for different sets of samples and genes depending on the hypothesis tested. We considered either RNA or proteins as outcome and the other phenotypes as mediators, and only genes found associated at FDR 5% (i.e., 2,518 eGenes and 329 pGenes). Samples were matched in each pairwise comparison. Considering SV-eQTLs as the outcome and SV-haQTLs as the mediator, 401 samples were analyzed (had RNA-seq and H3K9ac data available) and for each one of the 2,518 eGenes, H3K9ac peaks in 100 kb of the gene were tested as mediators. Similarly, for mediation by SV-sQTLs, a total of 433 samples were analyzed and any splicing junction in 100 kb of the gene were tested. We also tested the mediation of SV-eQTLs via SV-pQTLs. For that 112 samples were included and genes within 1 Mb of the eGene were tested as mediators. Analogously, we considered SV-pQTLs as outcome and SV-eQTLs as mediators, 112 samples and 311 genes (pGenes) were analyzed. For SV-pQTL as outcome and SV-haQTL as mediator, 124 samples and 329 genes were analyzed and any H3K9ac peak in 100 kb of the gene was tested as mediator. And finally for SV-pQTL as outcome and SV-sQTL as mediator, 135 samples and 329 genes, and any splicing junction in 100 kb of the gene was tested as mediator.

Expression outliers assessment

To identify expression outliers, either at RNA and protein levels, we used the *OUTRIDER* R package[88]. Briefly, data normalization was first performed using its inbuilt autoencoder method to control for variation linked to unknown factors. Then outlier detection was performed assuming a significant deviation of gene expression distributions from a negative binomial distribution. For the RNA, read counts for 15,004 genes expressed in 456 samples were used as input. While for proteins, we used the rounded batch adjusted abundances for 8,179 proteins and 272 samples. Samples with missing protein abundance values were imputed as the mean values of each protein. Since the observed protein variance across samples was considerably higher than for RNA, the number of outliers detected for proteins tended to be higher, so to control for this difference the significance threshold for outlier detection was set at FDR adjusted *P*-values of 0.05 and 0.001 for RNA and protein respectively and absolute z-scores higher than 2 for both data. A total of 1,551 gene-sample pairs outliers were identified in RNA, and 1,747 in proteins at the given thresholds.

Enrichment analysis

All enrichments of SV features were accessed via logistic regression as described elsewhere[50] and adjusted by SV size. This analysis is equivalent to the relative risk of

an SV having a specific feature (e.g., is overlapping a particular genomic annotation) given a secondary status (e.g., is SV-eQTL). Briefly, data were converted to a binary matrix with lines representing each SV and columns representing related features. Logistic regression was then performed fitting a generalized linear model (*glm* R function) and log odds ratio estimates and *P*-values were extracted from each feature comparison. The asymptotic distribution of the log relative risk was then used to obtain 95% Wald confidence intervals.

SVs tagging GWAS associated SNPs

SNPs mapped in high LD ($r^2 > 0.8$) with SVs were overlapped with a list of GWAS SNPs. We used the EBI GWAS catalog (release 2019–05-03) and matched SNPs by their reference number (rsID). A total 802 SVs were in LD with some GWAS SNPs (*P*-value $< 5 \times 10^{-8}$) and at LD $r^2 > 0.8$.

Disease status associations

SV calls from ROS/MAP, Mayo Clinic and MSBB were merged into a combined call set using *SURVIVOR*[75] while requiring 1000 bp maximum distance between breakpoints to merge SVs of the same type. A total of 22,007 SVs identified and all three study groups and with MAF ≥ 0.01 were selected for the association test. Alzheimer's disease status was harmonized across cohorts as previously described[89]. Briefly, for the ROSMAP study, late-onset AD (LOAD) cases were defined as individuals with a Braak neurofibrillary tangle (NFT) score ≥ 4, CERAD score ≤ 2, and a cognitive diagnosis of probable AD with no other causes, while individuals with Braak less ≤ 3, CERAD score ≥ 3, and cognitive diagnosis of "no cognitive impairment" were considered as controls. For MSBB, individuals CDR score ≥ 1, Braak score ≥ 4, and CERAD neuritic and cortical plaque score ≥ 2 were considered LOAD cases, while CDR scores ≤ 0.5, Braak ≤ 3, and CERAD ≤ 1 were considered controls (note that CERAD definitions differ between ROSMAP and MSBB studies). For the Mayo Clinic study, cases were defined based on neuropathology, with LOAD cases being individuals with Braak score ≥ 4 and CERAD neuritic and cortical plaque score > 1 while controls were defined as Braak ≤ 3, and CERAD < 2. A logistic regression was fitted using 539 AD cases and 368 controls and adjusting for sex, study, and the first three ancestry principal components. For PSP associations, Mayo Clinic study had 83 cases[90] with pathological diagnosis at autopsy were compared against the same 368 controls using the same model.

RESOURCE AVAILABILITY

Code Availability

All code used in this study has been provided in a single repository on GitHub (https://github.com/RajLabMSSM/AMP_AD_StructuralVariation).

Data Availability

Data supporting the findings of this study are available via the AD Knowledge Portal (https://adknowledgeportal.org). The AD Knowledge Portal is a platform for accessing data, analyses, and tools generated by the Accelerating Medicines Partnership (AMP-AD) Target Discovery Program and other National Institute on Aging (NIA)-supported

programs to enable open-science practices and accelerate translational learning. The data, analyses and tools are shared early in the research cycle without a publication embargo on secondary use. Data is available for general research use according to the following requirements for data access and data attribution (https://adknowledgeportal.org/DataAccess/Instructions). For access to content described in this manuscript, including raw PacBio long-read sequencing data, individual-level SV calls and SV-xQTL summary statistics see: www.doi.org/10.7303/syn26952206. Additionally, individual-level genotyping and SV-xQTL summary statistics data are also being made available through NIAGADS (Accession Number: NG00118). All SV site-frequency data from 1,706 donors discovered separately in each cohort, complete nominal and permuted SV-xQTL summary statistics, and disease status association summary statistics are publicly available on GitHub (https://github.com/RajLabMSSM/AMP_AD_StructuralVariation). The raw whole-genome sequence data used for SV discovery are available for each cohort respectively: ROS/MAP[26] (syn10901595); MSBB[29] (syn10901600) and Mayo Clinic[28] (syn10901601). ROS/MAP H3K9ac ChIP-seq data are available at syn4896408 and TMT proteomics data are available at syn17015098. RNA-seq reprocessed data from all cohorts were obtained from the RNAseq harmonization study[89] (syn9702085). Splicing junction proportions were obtained from Raj et al.[86] and a respective sQTL visualization (Shiny App) browser is available at https://rajlab.shinyapps.io/sQTLviz_ROSMAP/. ROS/MAP data can also be requested at https://www.radc.rush.edu.

METHODS & SUPPLEMENTAL INFORMATION

Detailed methods and supplemental information for this manuscript has been provided online.

Extended Data

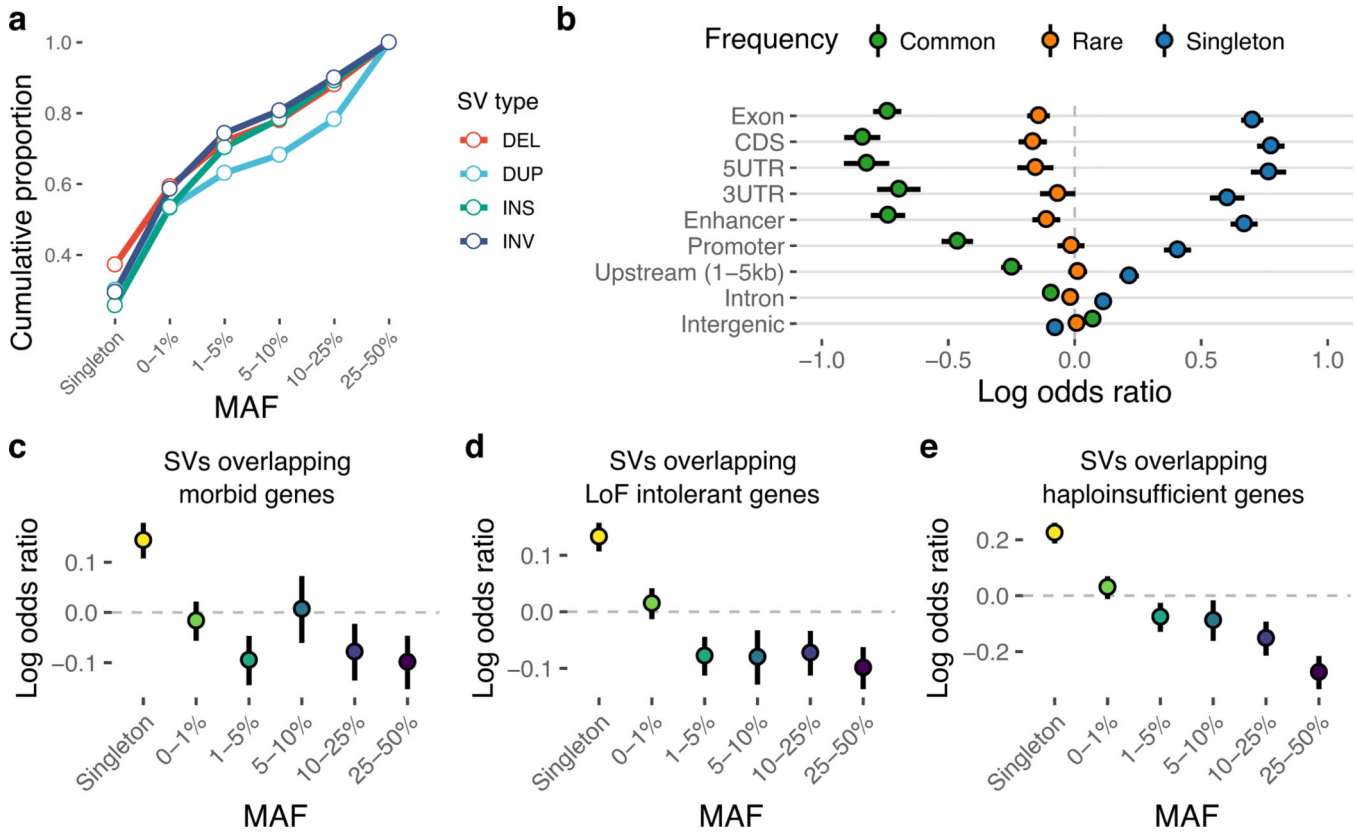

Extended Data Fig. 1. Functional context and evolutionary constraints

a, Cumulative fraction of SVs by minor allele frequency (MAF). **b**, Enrichment of SVs overlapping each region stratified by common (MAF>5%), rare (MAF<5%), and singleton. Enrichment of OMIM genes (**c**), LoF intolerant genes (**d**), and Haploinsufficient genes (**e**) overlapping SVs in different frequency stratum. Lines in the enrichment plots indicate Wald confidence intervals while the midpoints represent the relative log odds.

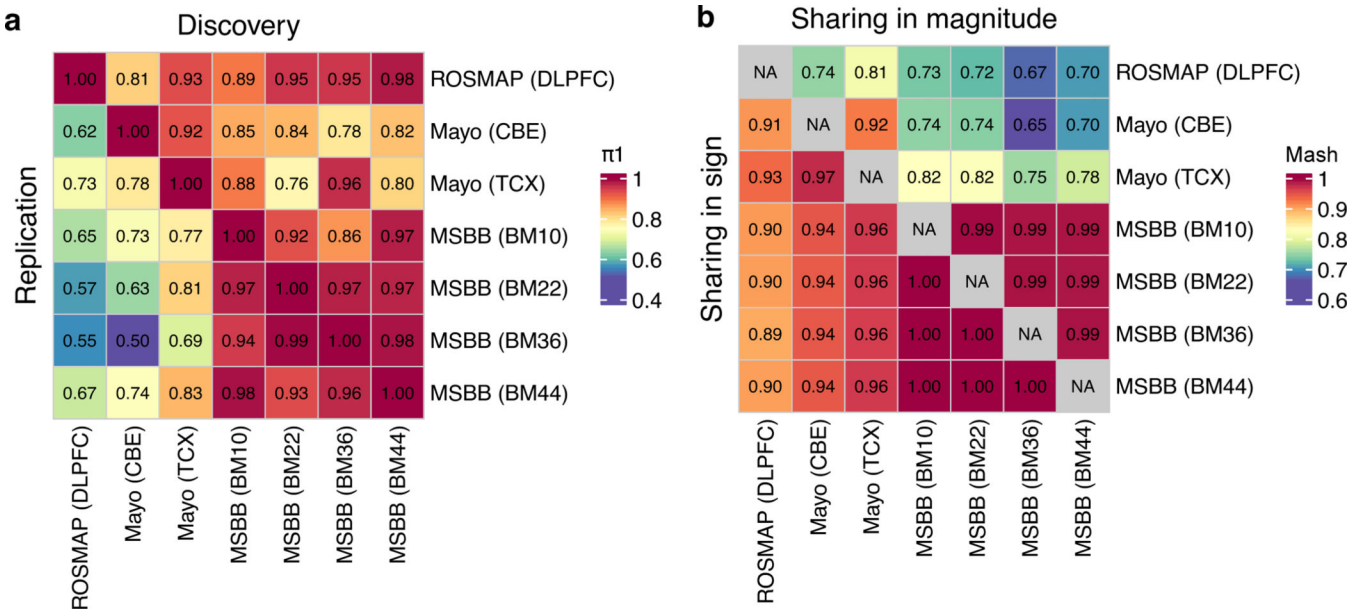

Extended Data Fig. 2. Pairwise sharing of eQTLs among brain tissues and cohorts

a, SV-eQTL sharing across different groups and regions measured by π1 from qvalue R package. Columns represent the discovery sets while rows represent the replication set. **b**, Sharing according to mashR meta-analysis. SV-eQTLs with local false sign rate (lfsr) lower than 0.05 in at least one of the two tissues were considered (n = 1,081–1,364 gene-SV pairs, depending on pair of tissues compared). Lower triangle shows the proportion of sharing by sign (i.e. effect estimates have the same direction). Upper triangle shows the proportion of sharing in magnitude (i.e. effect estimates that are in the same direction and within a factor of 2 in size).

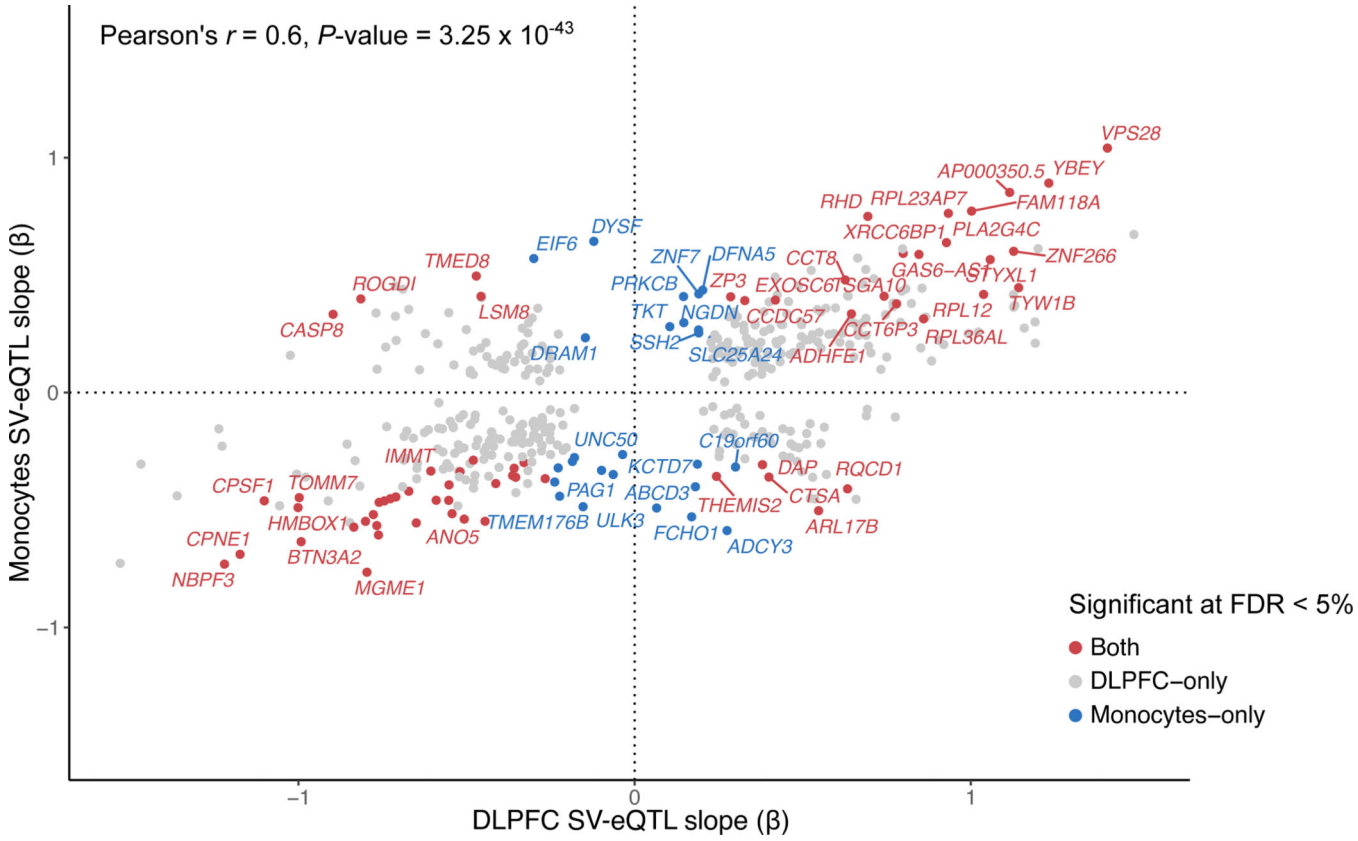

Extended Data Fig. 3. Comparison between brain and monocytes SV-eQTLs effect sizes

Scatter plot shows the slope of 429 eGenes mapped in ROS/MAP DLPFC and Monocytes with a significant association in either dataset (FDR < 5%). Although majority of effects are concordant in direction, many genes show opposite direction of effects between brain and monocytes (e.g. *ARL17B* and *CASP8*). The x-axis shows the effect size in DLPFC and y-axis shows the effect size in Monocytes for the same SV-gene pair. Dots colored in blue are significant only at Monocytes, dots colored in grey are significant only in DLPFC, and dots in red are significant in both. Pearson correlation coefficient (and *P*-value, two-sided) of slopes for all 144 SV-gene pairs is shown on top.

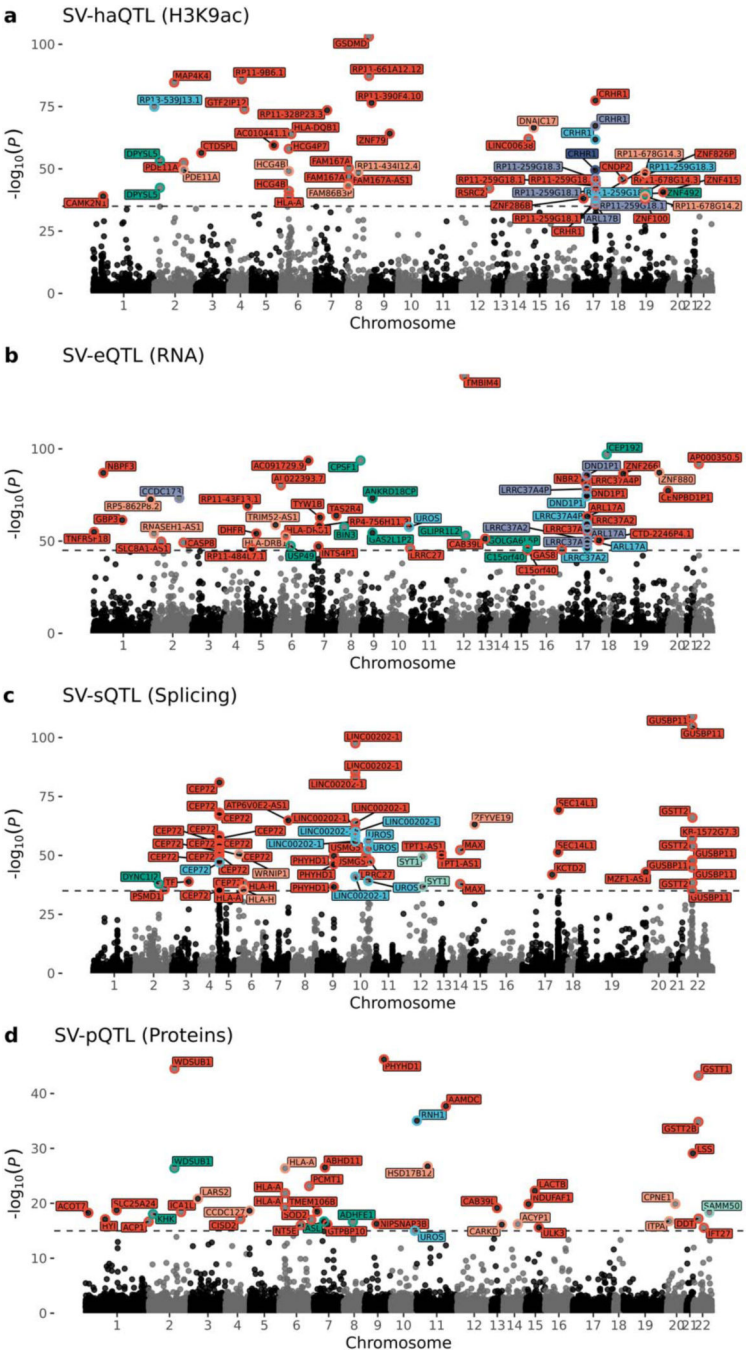

Extended Data Fig. 4. SV-xQTL top hits

Manhattan plots showing the top SV-xQTLs measured in ROS/MAP. Colored labels represent each SV class. **a**, SV-haQTL (H3K9ac), showing labels for associations with -$\log_{10}$(*P*-value)>30. **b**, SV-eQTL, labels for associations with -$\log_{10}$(*P*-value)>40. **c**, SV-sQTL, labels for associations with -$\log_{10}$(*P*-value)>40. **d**, SV-pQTL, labels for associations with -$\log_{10}$(*P*-value)>10.

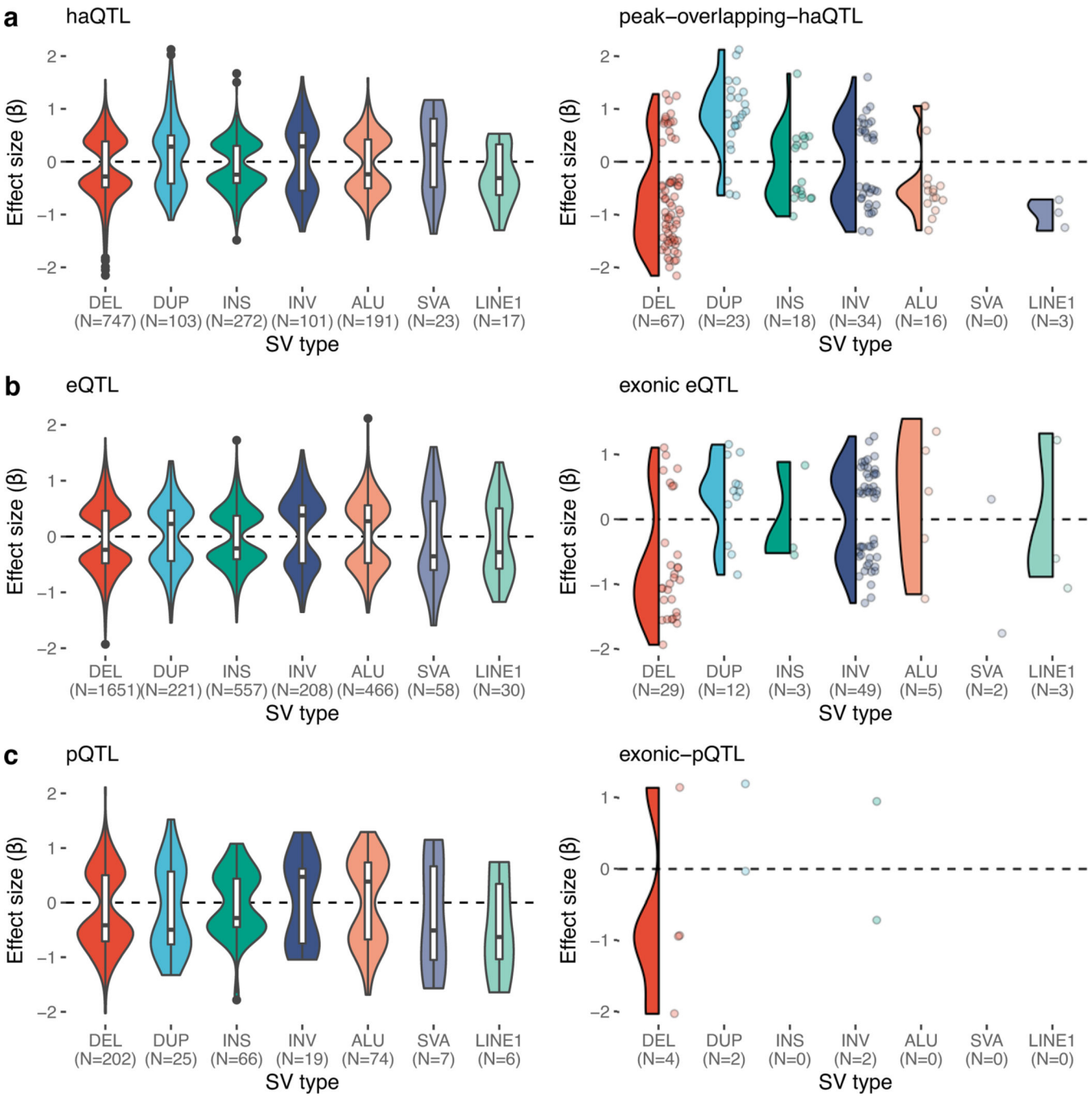

Extended Data Fig. 5. SV-xQTL effect sizes

Distribution of effect sizes for all SVx-QTLs by SV class. Plots on the left show results for all associated SVs, plots on the right show results only for SVs overlapping either the associated histone peak (SV-haQTL, **a**), or exonic regions of the associated gene (SV-eQTL on **b** and SV-pQTL on **c**).

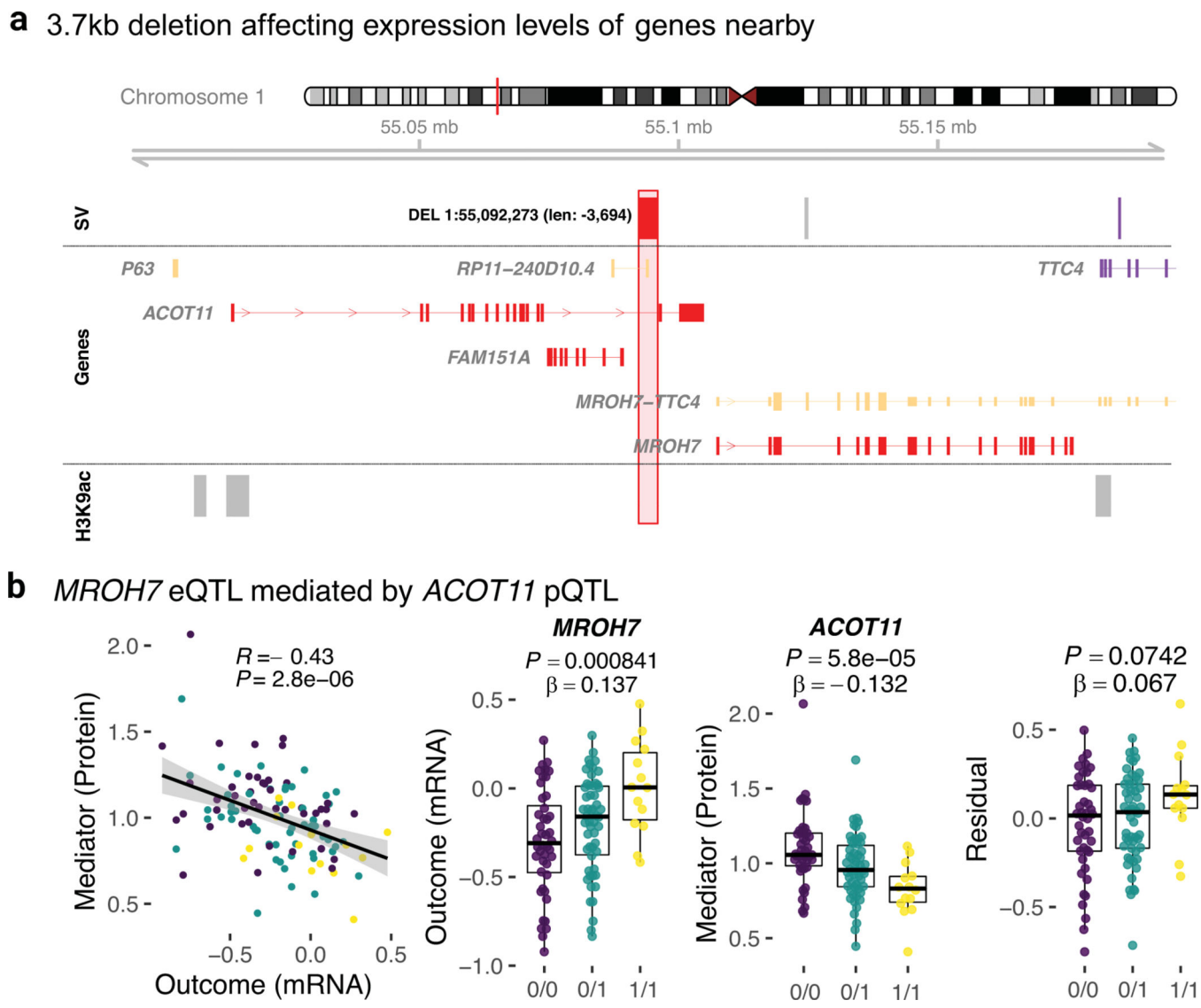

Extended Data Fig. 6. SV-eQTL mediation by SV-pQTL

a, The locus plot shows a 3.7 kb deletion (in red) deleting the splicing acceptor sites on exon 16 of the gene *ACOT11* (from which is an SV-eQTL and SV-pQTL). Genes and histone peaks colored in red had significant associations (FDR < 0.05) with the SV. **b**, Mediation analysis performed on 112 biologically independent samples with both RNA-seq and proteomics data available, supports the mediation of the gene *MROH7* SV-eQTL via SV-pQTL of *ACOT11* (complete mediation posterior probability = 0.59). The scatter plot on the left shows the correlation between both phenotypes, x-axis is the residual mRNA expression of *MROH7* while the y-axis is the residual protein abundance levels for *ACOT11*. Pearson correlation coefficient (R) and respective *P*-value as well as a linear regression line are shown in the plot. The box plots show the median in the central line, the box spans the first to the third quartiles and the whiskers extend 1.5 times the IQR from the box. Nominal *P*-values and effect sizes from the linear regression model are listed on the top of each box plot.

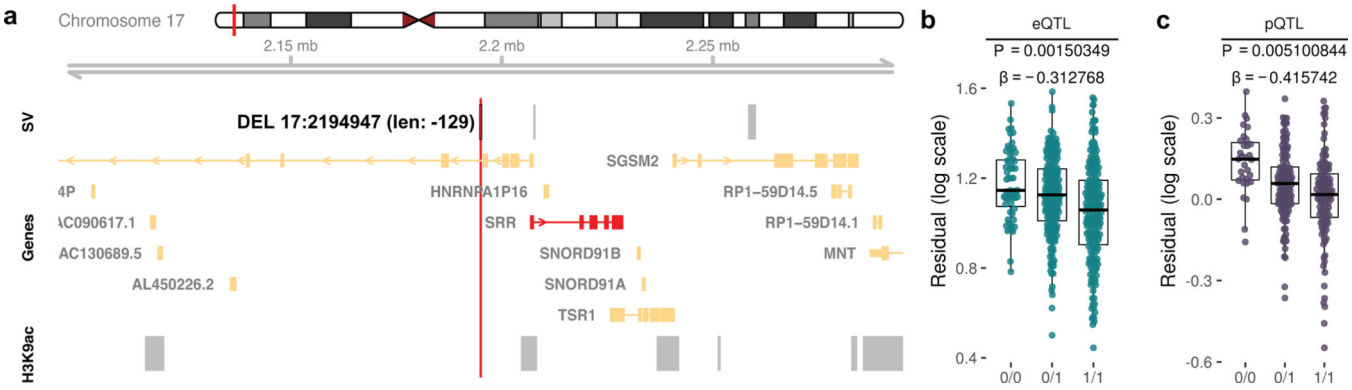

Extended Data Fig. 7. SV-xQTL in LD with Schizophrenia GWAS variant

a, locus plot showing a 129 bp deletion that is in LD with a Schizophrenia GWAS variant (rs8070345, $R^2 = 0.94$)[6]. Plot also shows genes and H3K9ac peaks near the SV. Genes colored in red represent phenotypes found significantly associated with the deletion at RNA and protein levels (SV-eQTL and SV-pQTL at FDR < 5%). **b**, shows the boxplot for the SV-eQTL association with the gene *SRR* (n = 456 biologically independent samples), **c**, shows the boxplot for the SV-pQTL association with the gene *SRR* (n = 272 biologically independent samples). In the box plots, slopes (β) and FDR adjusted *P*-values are shown for each association (linear regression model), the median values are shown in the central line, the box spans the first to the third quartiles and the whiskers extend 1.5 times the IQR from the box.

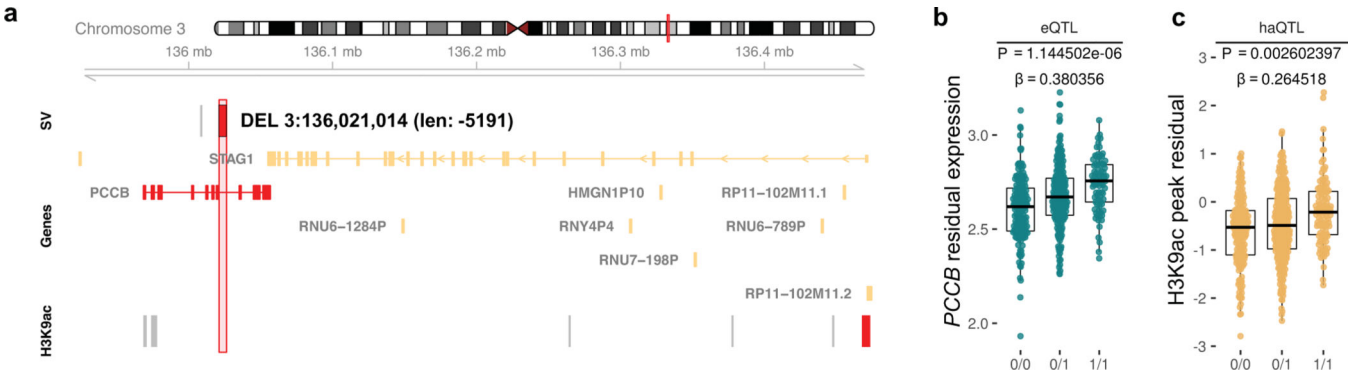

Extended Data Fig. 8. SV-xQTL in LD with Schizophrenia GWAS variant

a, locus plot showing a 5191 bp deletion that is in LD with a Schizophrenia GWAS variant (rs66691851, $R^2 = 0.95$)[6]. Plot also shows genes and H3K9ac peaks near the SV. Genes and H3K9ac bars colored in red represent phenotypes found significantly associated with the deletion (SV-eQTL and SV-haQTL at FDR < 5%). **b**, shows the boxplot for the SV-eQTL association for the *PCCB* (n = 456 biologically independent samples), **c**, shows the boxplot for the SV-haQTL association for a peak in the promoter region of *STAG1* (n = 571 biologically independent samples). In the box plots, slopes (β) and FDR adjusted *P*-values are shown for each association (linear regression model), the median values are shown in the central line, the box spans the first to the third quartiles and the whiskers extend 1.5 times the IQR from the box.

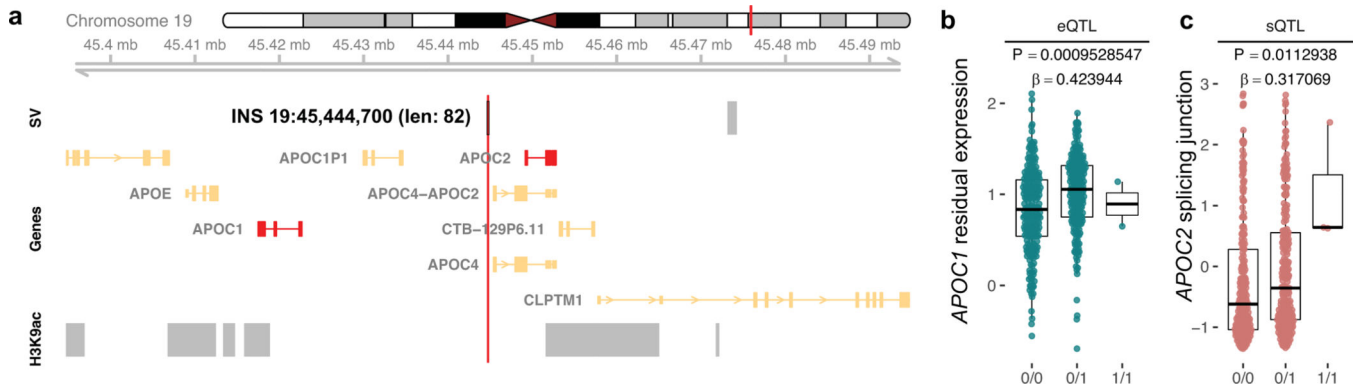

Extended Data Fig. 9. SV-xQTL in LD with Alzheimer's disease GWAS variant

a, locus plot showing a 82 bp insertion that is in LD with an Alzheimer's disease GWAS variant (rs73045691, $R^2 = 0.80$)[6]. Plot also shows genes and H3K9ac peaks near the SV. Genes colored in red represent phenotypes found significantly associated with the insertion (SV-eQTL and SV-sQTL at FDR < 5%). **b**, shows the boxplot for the SV-eQTL association for the *APOC1* gene (n = 456 biologically independent samples), **c**, shows the boxplot for the SV-sQTL association for a peak in the promoter region of *APOC2* (n = 505 biologically independent samples). In the box plots, slopes (β) and FDR adjusted *P*-values are shown for each association (linear regression model), the median values are shown in the central line, the box spans the first to the third quartiles and the whiskers extend 1.5 times the IQR from the box.

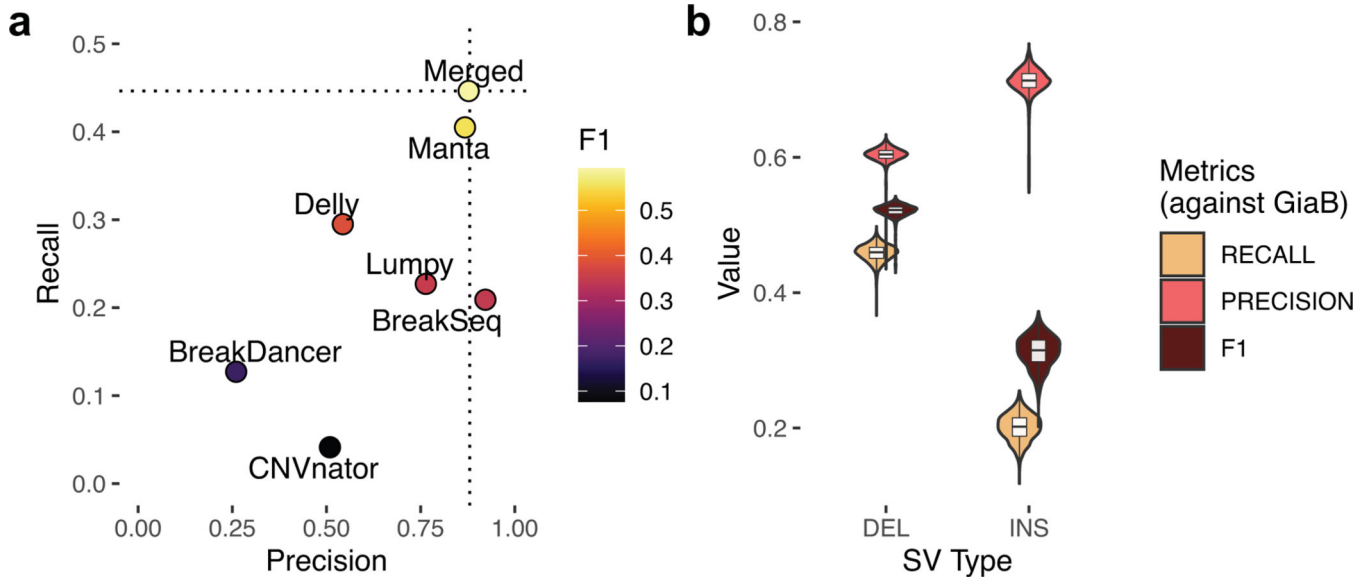

Extended Data Fig. 10. Quality assessment of variant calling

In silico benchmarking and validation. **a**, Benchmarking of individual SV discovery tools and combined tools ("Merged") for the sample HG002 evaluated against the Genome in a Bottle v0.6 Tier 1 using *truvari*. "Merged" strategy was defined by the best F1-score after testing all possible combinations of tools (for insertions and deletions separately). The same merging criteria was applied for all samples in AMP-AD. **b**, Benchmarking results of all

1,760 AMP-AD samples evaluated against the Genome in a Bottle v0.6 Tier 1 using *truvari*. In the box plots, the median values are shown in the central line, the box spans the first to the third quartiles and the whiskers extend 1.5 times the IQR from the box.

Supplementary Material

Refer to Web version on PubMed Central for supplementary material.

ACKNOWLEDGMENTS

We thank the participants of AMP-AD cohorts for their essential contributions and gift to these projects. ROSMAP study data were provided by the Rush Alzheimer's Disease Center, Rush University Medical Center, Chicago. Data collection was supported through funding by National Institute on Aging (NIA) grants P30AG10161, R01AG15819, R01AG17917, R01AG30146, R01AG36836, U01AG32984, U01AG46152, U01AG61356, and the Illinois Department of Public Health. Mayo RNA-seq study data were provided by the following sources: the Mayo Clinic Alzheimer's Disease Genetic Studies, led by Dr. Nilufer Ertekin-Taner and Dr. Steven G. Younkin, Mayo Clinic, Jacksonville, Florida, using samples from the Mayo Clinic Study of Aging, the Mayo Clinic Alzheimer's Disease Research Center, and the Mayo Clinic Brain Bank. Data collection was supported through funding by NIA grants P50 AG016574, R01 AG032990, U01 AG046139, R01 AG018023, U01 AG006576, U01 AG006786, R01 AG025711, R01 AG017216, and R01 AG003949; National Institute of Neurological Disorders and Stroke (NINDS) grant R01 NS080820; the CurePSP Foundation; and support from Mayo Foundation. Study data include samples collected through the Sun Health Research Institute Brain and Body Donation Program of Sun City, Arizona. The Brain and Body Donation Program is supported by the National Institute of Neurological Disorders and Stroke (U24 NS072026, National Brain and Tissue Resource for Parkinson's Disease and Related Disorders), the NIA (P30 AG19610, Arizona Alzheimer's Disease Core Center), the Arizona Department of Health Services (contract 211002, Arizona Alzheimer's Research Center), the Arizona Biomedical Research Commission (contracts 4001, 0011, 05-901, and 1001 to the Arizona Parkinson's Disease Consortium), and the Michael J. Fox Foundation for Parkinson's Research. Mount Sinai Brain Bank (MSBB) data were generated from post-mortem brain tissue collected through the Mount Sinai VA Medical Center Brain Bank and were provided by Dr. Eric Schadt of the Mount Sinai School of Medicine through funding from NIA grant U01AG046170. The authors thank Dr. Bin Zhang and Dr. Erming Wang for assistance with data sharing, and members of the Raj and Crary labs for their feedback on the manuscript. We thank Jack Humphrey for his insightful comments and suggestions during this work. This work was supported by grants from the US National Institutes of Health (NIH NIA U01-AG068880, NIA R01-AG054005, NIA R56-AG055824, and NIA R01-AG054008). This work was supported in part through the computational and data resources and staff expertise provided by Scientific Computing at the Icahn School of Medicine at Mount Sinai. We thank the Mount Sinai Technology Development core for help and support with performing long-read sequencing. Cartoons in the figures 1, 5b and 5c were created with BioRender.com. The research reported in this paper was supported by the Office of Research Infrastructure of the National Institutes of Health under award number S10OD026880. The funders had no role in study design, data collection and analysis, decision to publish or preparation of the manuscript.

REFERENCES

1. Sudmant PH et al. An integrated map of structural variation in 2,504 human genomes. Nature 526, 75–81 (2015). [PubMed: 26432246]
2. Abel HJ et al. Mapping and characterization of structural variation in 17,795 human genomes. Nature 583, 83–89 (2020). [PubMed: 32460305]
3. Collins RL et al. A structural variation reference for medical and population genetics. Nature 581, 444–451 (2020). [PubMed: 32461652]
4. Feuk L, Carson AR & Scherer SW Structural variation in the human genome. Nat. Rev. Genet. 7, 85–97 (2006). [PubMed: 16418744]
5. Sharp AJ, Cheng Z. & Eichler EE Structural variation of the human genome. Annu. Rev. Genomics Hum. Genet. 7, 407–442 (2006). [PubMed: 16780417]
6. Conrad DF et al. Origins and functional impact of copy number variation in the human genome. Nature 464, 704–712 (2010). [PubMed: 19812545]
7. Ebert P. et al. Haplotype-resolved diverse human genomes and integrated analysis of structural variation. Science 372, (2021).

8. Byrska-Bishop M. et al. High coverage whole genome sequencing of the expanded 1000 Genomes Project cohort including 602 trios. bioRxiv (2021) doi:10.1101/2021.02.06.430068.
9. Chaisson MJP et al. Multi-platform discovery of haplotype-resolved structural variation in human genomes. Nat. Commun. 10, 1784 (2019). [PubMed: 30992455]
10. McCarthy SE et al. Microduplications of 16p11.2 are associated with schizophrenia. Nat. Genet. 41, 1223–1227 (2009). [PubMed: 19855392]
11. Sekar A. et al. Schizophrenia risk from complex variation of complement component 4. Nature 530, 177–183 (2016). [PubMed: 26814963]
12. Marshall CR et al. Contribution of copy number variants to schizophrenia from a genome-wide study of 41,321 subjects. Nat. Genet. 49, 27–35 (2017). [PubMed: 27869829]
13. Pinto D. et al. Functional impact of global rare copy number variation in autism spectrum disorders. Nature 466, 368–372 (2010). [PubMed: 20531469]
14. Sebat J. et al. Strong association of de novo copy number mutations with autism. Science 316, 445–449 (2007). [PubMed: 17363630]
15. Mitra I. et al. Patterns of de novo tandem repeat mutations and their role in autism. Nature 589, 246–250 (2021). [PubMed: 33442040]
16. Männik K. et al. Copy number variations and cognitive phenotypes in unselected populations. JAMA 313, 2044–2054 (2015). [PubMed: 26010633]
17. Stefansson H. et al. CNVs conferring risk of autism or schizophrenia affect cognition in controls. Nature 505, 361–366 (2014). [PubMed: 24352232]
18. Battle A. et al. Impact of regulatory variation from RNA to protein. Science 347, 664–667 (2015). [PubMed: 25657249]
19. Li YI et al. RNA splicing is a primary link between genetic variation and disease. Science 352, 600–604 (2016). [PubMed: 27126046]
20. Ng B. et al. An xQTL map integrates the genetic architecture of the human brain's transcriptome and epigenome. Nat. Neurosci. 20, 1418–1426 (2017). [PubMed: 28869584]
21. Chiang C. et al. The impact of structural variation on human gene expression. Nat. Genet. 49, 692–699 (2017). [PubMed: 28369037]
22. Scott AJ, Chiang C. & Hall IM Structural variants are a major source of gene expression differences in humans and often affect multiple nearby genes. Genome Res. gr.275488.121 (2021).
23. Ramsköld D, Wang ET, Burge CB & Sandberg R. An abundance of ubiquitously expressed genes revealed by tissue transcriptome sequence data. PLoS Comput. Biol. 5, e1000598 (2009).
24. Polymenidou M. et al. Long pre-mRNA depletion and RNA missplicing contribute to neuronal vulnerability from loss of TDP-43. Nat. Neurosci. 14, 459–468 (2011). [PubMed: 21358643]
25. Sonawane AR et al. Understanding Tissue-Specific Gene Regulation. Cell Rep. 21, 1077–1088 (2017). [PubMed: 29069589]
26. De Jager PL et al. A multi-omic atlas of the human frontal cortex for aging and Alzheimer's disease research. Sci Data 5, 180142 (2018).
27. Bennett DA et al. Religious Orders Study and Rush Memory and Aging Project. J. Alzheimers. Dis. 64, S161–S189 (2018). [PubMed: 29865057]
28. Allen M. et al. Human whole genome genotype and transcriptome data for Alzheimer's and other neurodegenerative diseases. Sci Data 3, 160089 (2016).
29. Wang M. et al. The Mount Sinai cohort of large-scale genomic, transcriptomic and proteomic data in Alzheimer's disease. Scientific Data vol. 5 (2018).
30. Hodes RJ & Buckholtz N. Accelerating medicines partnership: Alzheimer's disease (AMP-AD) knowledge portal aids Alzheimer's drug discovery through open data sharing. Expert Opin. Ther. Targets 20, 389–391 (2016). [PubMed: 26853544]
31. Lappalainen I. et al. DbVar and DGVa: public archives for genomic structural variation. Nucleic Acids Res. 41, D936–41 (2013). [PubMed: 23193291]
32. MacDonald JR, Ziman R, Yuen RKC, Feuk L. & Scherer SW The Database of Genomic Variants: a curated collection of structural variation in the human genome. Nucleic Acids Res. 42, D986–92 (2014). [PubMed: 24174537]

33. Firth HV, Wright CF & DDD Study. The Deciphering Developmental Disorders (DDD) study. Dev. Med. Child Neurol. 53, 702–703 (2011). [PubMed: 21679367]
34. Han L. et al. Functional annotation of rare structural variation in the human brain. doi:10.1101/711754.
35. Jakubosky D. et al. Properties of structural variants and short tandem repeats associated with gene expression and complex traits. Nat. Commun. 11, 2927 (2020). [PubMed: 32522982]
36. Lek M. et al. Analysis of protein-coding genetic variation in 60,706 humans. Nature 536, 285–291 (2016). [PubMed: 27535533]
37. Urbut SM, Wang G, Carbonetto P. & Stephens M. Flexible statistical methods for estimating and testing effects in genomic studies with multiple conditions. Nat. Genet. 51, 187–195 (2019). [PubMed: 30478440]
38. Hormozdiari F, Kostem E, Kang EY, Pasaniuc B. & Eskin E. Identifying causal variants at loci with multiple signals of association. Genetics 198, 497–508 (2014). [PubMed: 25104515]
39. Shi Y. et al. Common variants on 8p12 and 1q24.2 confer risk of schizophrenia. Nat. Genet. 43, 1224–1227 (2011). [PubMed: 22037555]
40. Kondrashov FA & Koonin EV Origin of alternative splicing by tandem exon duplication. Hum. Mol. Genet. 10, 2661–2669 (2001). [PubMed: 11726553]
41. Han L. et al. Functional annotation of rare structural variation in the human brain. Nature Communications vol. 11 (2020).
42. Sieberts SK et al. Large eQTL meta-analysis reveals differing patterns between cerebral cortical and cerebellar brain regions. Sci. Data 7, 340 (2020). [PubMed: 33046718]
43. Lev-Maor G. et al. Intronic Alus influence alternative splicing. PLoS Genet. 4, e1000204 (2008).
44. Ade C, Roy-Engel AM & Deininger PL Alu elements: an intrinsic source of human genome instability. Curr. Opin. Virol. 3, 639–645 (2013). [PubMed: 24080407]
45. Kim DS & Hahn Y. Identification of human-specific transcript variants induced by DNA insertions in the human genome. Bioinformatics 27, 14–21 (2011). [PubMed: 21037245]
46. Hancks DC, Ewing AD, Chen JE, Tokunaga K. & Kazazian HH Jr. Exon-trapping mediated by the human retrotransposon SVA. Genome Res. 19, 1983–1991 (2009). [PubMed: 19635844]
47. Crouse WL, Keele GR, Gastonguay MS, Churchill GA & Valdar W. A Bayesian model selection approach to mediation analysis. bioRxiv (2021) doi:10.1101/2021.07.19.452969.
48. Robins C. et al. Genetic control of the human brain proteome. Am. J. Hum. Genet. 108, 400–410 (2021). [PubMed: 33571421]
49. Ferraro NM et al. Transcriptomic signatures across human tissues identify functional rare genetic variation. Science vol. 369 eaaz5900 (2020).
50. Li X. et al. The impact of rare variation on gene expression across tissues. Nature 550, 239–243 (2017). [PubMed: 29022581]
51. Schizophrenia Working Group of the Psychiatric Genomics Consortium. Biological insights from 108 schizophrenia-associated genetic loci. Nature 511, 421–427 (2014). [PubMed: 25056061]
52. Nalls MA et al. Large-scale meta-analysis of genome-wide association data identifies six new risk loci for Parkinson's disease. Nat. Genet. 46, 989–993 (2014). [PubMed: 25064009]
53. Höglinger GU et al. Identification of common variants influencing risk of the tauopathy progressive supranuclear palsy. Nat. Genet. 43, 699–705 (2011). [PubMed: 21685912]
54. Chen JA et al. Joint genome-wide association study of progressive supranuclear palsy identifies novel susceptibility loci and genetic correlation to neurodegenerative diseases. Molecular Neurodegeneration vol. 13 (2018).
55. Corces MR et al. Single-cell epigenomic analyses implicate candidate causal variants at inherited risk loci for Alzheimer's and Parkinson's diseases. Nat. Genet. 52, 1158–1168 (2020). [PubMed: 33106633]
56. Wenger AM et al. Accurate circular consensus long-read sequencing improves variant detection and assembly of a human genome. Nat. Biotechnol. (2019) doi:10.1038/s41587-019-0217-9.
57. Vogel C. & Marcotte EM Insights into the regulation of protein abundance from proteomic and transcriptomic analyses. Nat. Rev. Genet. 13, 227–232 (2012). [PubMed: 22411467]

58. Jacques P-É, Jeyakani J. & Bourque G. The majority of primate-specific regulatory sequences are derived from transposable elements. PLoS Genet. 9, e1003504 (2013).
59. Kellner M. & Makałowski W. Transposable elements significantly contributed to the core promoters in the human genome. Sci. China Life Sci. 62, 489–497 (2019). [PubMed: 30915629]
60. Bennett EA, Coleman LE, Tsui C, Pittard WS & Devine SE Natural genetic variation caused by transposable elements in humans. Genetics 168, 933–951 (2004). [PubMed: 15514065]
61. Kwon Y-J et al. Structure and Expression Analyses of SVA Elements in Relation to Functional Genes. Genomics Inform. 11, 142–148 (2013). [PubMed: 24124410]
62. Gianfrancesco O. et al. The Role of SINE-VNTR-Alu (SVA) Retrotransposons in Shaping the Human Genome. Int. J. Mol. Sci. 20, (2019).
63. Savage AL, Bubb VJ, Breen G. & Quinn JP Characterisation of the potential function of SVA retrotransposons to modulate gene expression patterns. BMC Evol. Biol. 13, 101 (2013). [PubMed: 23692647]
64. Savage AL et al. An evaluation of a SVA retrotransposon in the FUS promoter as a transcriptional regulator and its association to ALS. PLoS One 9, e90833 (2014).
65. Gianfrancesco O, Bubb VJ & Quinn JP SVA retrotransposons as potential modulators of neuropeptide gene expression. Neuropeptides 64, 3–7 (2017). [PubMed: 27743609]
66. Quinn JP & Bubb VJ SVA retrotransposons as modulators of gene expression. Mob. Genet. Elements 4, e32102 (2014).
67. Chander V, Gibbs RA & Sedlazeck FJ Evaluation of computational genotyping of structural variation for clinical diagnoses. Gigascience 8, (2019).

METHODS REFERENCES

68. Rausch T. et al. DELLY: structural variant discovery by integrated paired-end and split-read analysis. Bioinformatics 28, i333–i339 (2012). [PubMed: 22962449]
69. Layer RM, Chiang C, Quinlan AR & Hall IM LUMPY: a probabilistic framework for structural variant discovery. Genome Biol. 15, R84 (2014). [PubMed: 24970577]
70. Chen X. et al. Manta: rapid detection of structural variants and indels for germline and cancer sequencing applications. Bioinformatics 32, 1220–1222 (2016). [PubMed: 26647377]
71. Chen K. et al. BreakDancer: an algorithm for high-resolution mapping of genomic structural variation. Nat. Methods 6, 677–681 (2009). [PubMed: 19668202]
72. Abyzov A, Urban AE, Snyder M. & Gerstein M. CNVnator: an approach to discover, genotype, and characterize typical and atypical CNVs from family and population genome sequencing. Genome Res. 21, 974–984 (2011). [PubMed: 21324876]
73. Abyzov A. et al. Analysis of deletion breakpoints from 1,092 humans reveals details of mutation mechanisms. Nat. Commun. 6, 7256 (2015). [PubMed: 26028266]
74. Gardner EJ et al. The Mobile Element Locator Tool (MELT): population-scale mobile element discovery and biology. Genome Res. 27, 1916–1929 (2017). [PubMed: 28855259]
75. Jeffares DC et al. Transient structural variations have strong effects on quantitative traits and reproductive isolation in fission yeast. Nat. Commun. 8, 14061 (2017).
76. Geoffroy V. et al. AnnotSV: an integrated tool for structural variations annotation. Bioinformatics 34, 3572–3574 (2018). [PubMed: 29669011]
77. Graffelman J, Nelson S, Gogarten SM & Weir BS Exact Inference for Hardy-Weinberg Proportions with Missing Genotypes: Single and Multiple Imputation. G3 5, 2365–2373 (2015). [PubMed: 26377959]
78. Jiang T. et al. Long-read-based human genomic structural variation detection with cuteSV. Genome Biol. 21, 189 (2020). [PubMed: 32746918]
79. Li H. Minimap2: pairwise alignment for nucleotide sequences. Bioinformatics 34, 3094–3100 (2018). [PubMed: 29750242]
80. Heller D. & Vingron M. SVIM-asm: Structural variant detection from haploid and diploid genome assemblies. Bioinformatics (2020) doi:10.1093/bioinformatics/btaa1034.

81. Zhao X, Weber AM & Mills RE A recurrence-based approach for validating structural variation using long-read sequencing technology. Gigascience 6, 1–9 (2017).
82. Ongen H, Buil A, Brown AA, Dermitzakis ET & Delaneau O. Fast and efficient QTL mapper for thousands of molecular phenotypes. Bioinformatics 32, 1479–1485 (2016). [PubMed: 26708335]
83. Klein H-U et al. Epigenome-wide study uncovers large-scale changes in histone acetylation driven by tau pathology in aging and Alzheimer's human brains. Nat. Neurosci. 22, 37–46 (2019). [PubMed: 30559478]
84. Ping L. et al. Global quantitative analysis of the human brain proteome in Alzheimer's and Parkinson's Disease. Sci Data 5, 180036 (2018).
85. Johnson ECB et al. Deep proteomic network analysis of Alzheimer's disease brain reveals alterations in RNA binding proteins and RNA splicing associated with disease. Mol. Neurodegener. 13, 1–22 (2018). [PubMed: 29310663]
86. Raj T. et al. Integrative transcriptome analyses of the aging brain implicate altered splicing in Alzheimer's disease susceptibility. Nat. Genet. 50, 1584–1592 (2018). [PubMed: 30297968]
87. The GTEx Consortium. The GTEx Consortium atlas of genetic regulatory effects across human tissues. Science 369, 1318–1330 (2020). [PubMed: 32913098]
88. Brechtmann F. et al. OUTRIDER: A Statistical Method for Detecting Aberrantly Expressed Genes in RNA Sequencing Data. Am. J. Hum. Genet. 103, 907–917 (2018). [PubMed: 30503520]
89. Wan Y-W et al. Meta-Analysis of the Alzheimer's Disease Human Brain Transcriptome and Functional Dissection in Mouse Models. Cell Rep. 32, 107908 (2020).
90. Allen M. et al. Gene expression, methylation and neuropathology correlations at progressive supranuclear palsy risk loci. Acta Neuropathol. 132, 197–211 (2016). [PubMed: 27115769]

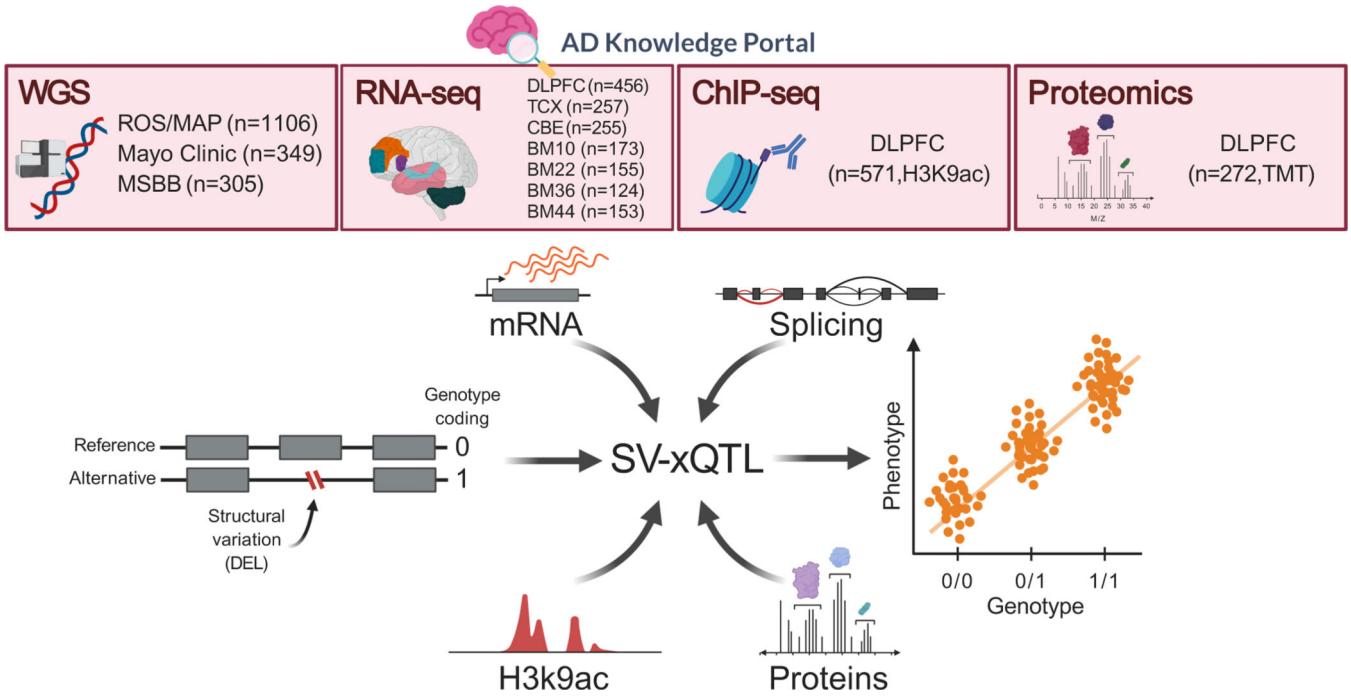

Figure 1. Study overview.

The datasets used in this study have been made available to the research community through the Accelerating Medicines Partnership in Alzheimer's Disease (AMP-AD) Knowledge Portal. Whole-genome sequencing and RNA-seq datasets are available from four aging and Alzheimer's disease cohorts: Religious Orders Study (ROS) and Memory and Aging Project (MAP), Mayo Clinic, and Mount Sinai Brain Bank (MSBB). RNA-seq data for ROS/MAP are from the dorsolateral prefrontal cortex (DLPFC). RNA-seq data from MSBB are from four brain regions: BM10 = Brodmann area 10 (part of the frontopolar prefrontal cortex), BM22 = Brodmann area 22 (part of the superior temporal gyrus), BM36 = Brodmann area 36 (part of the fusiform gyrus), and BM44 = Brodmann area 44 (opercular part of the inferior frontal gyrus). RNA-seq from Mayo Clinic are from TCX = temporal cortex, CBE = cerebellum. The ChIP-seq (Histone 3 Lysine 9 acetylation, H3K9Ac) and proteomics data (Tandem mass tag, TMT) are from ROS/MAP dorsolateral prefrontal cortex (DLPFC) tissues. The post-QC sample sizes are shown next to each dataset. eQTL analyses were performed in all datasets; sQTL, haQTL, and pQTL were only performed with ROS/MAP data.

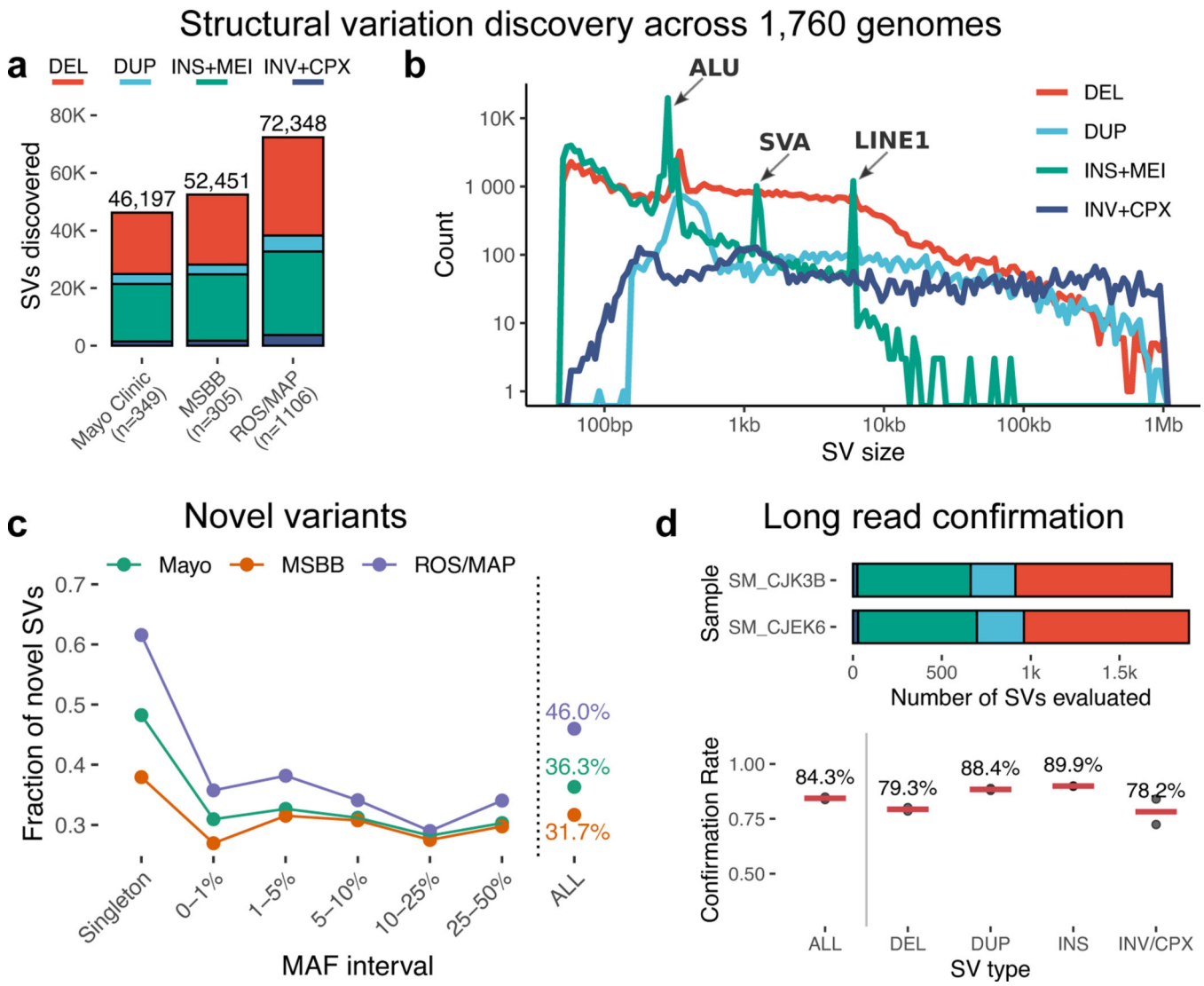

Figure 2 - Summary of SV calls across cohorts.

a, Total number of SVs identified within each cohort (ROS/MAP, Mayo Clinic, MSBB), colored by main SV types (DEL, DUP, INS+MEI, and INV+CPX). **b**, SV size distribution per SV type with x-axis and y-axis shown in $\log_{10}$ scale. **c**, Proportion of novel SVs found in each cohort stratified by minor allele frequency (MAF) spectrum. SVs were considered novel if not found in dbVar, Centers for Common Disease Genomics (CCDG), Database of Genomic Variants (DGV), Deciphering Developmental Disorders (DDD), GnomAD-SV, and the 1000 Genomes Project. **d**, Barplot showing samples sequenced using PacBio's long-read WGS and number of SVs from short-reads evaluated for replication, plot below shows the confirmation rates for each sample (dots) measured using *VaPoR* and stratified by each SV class. Horizontal bars represent the median of both samples.

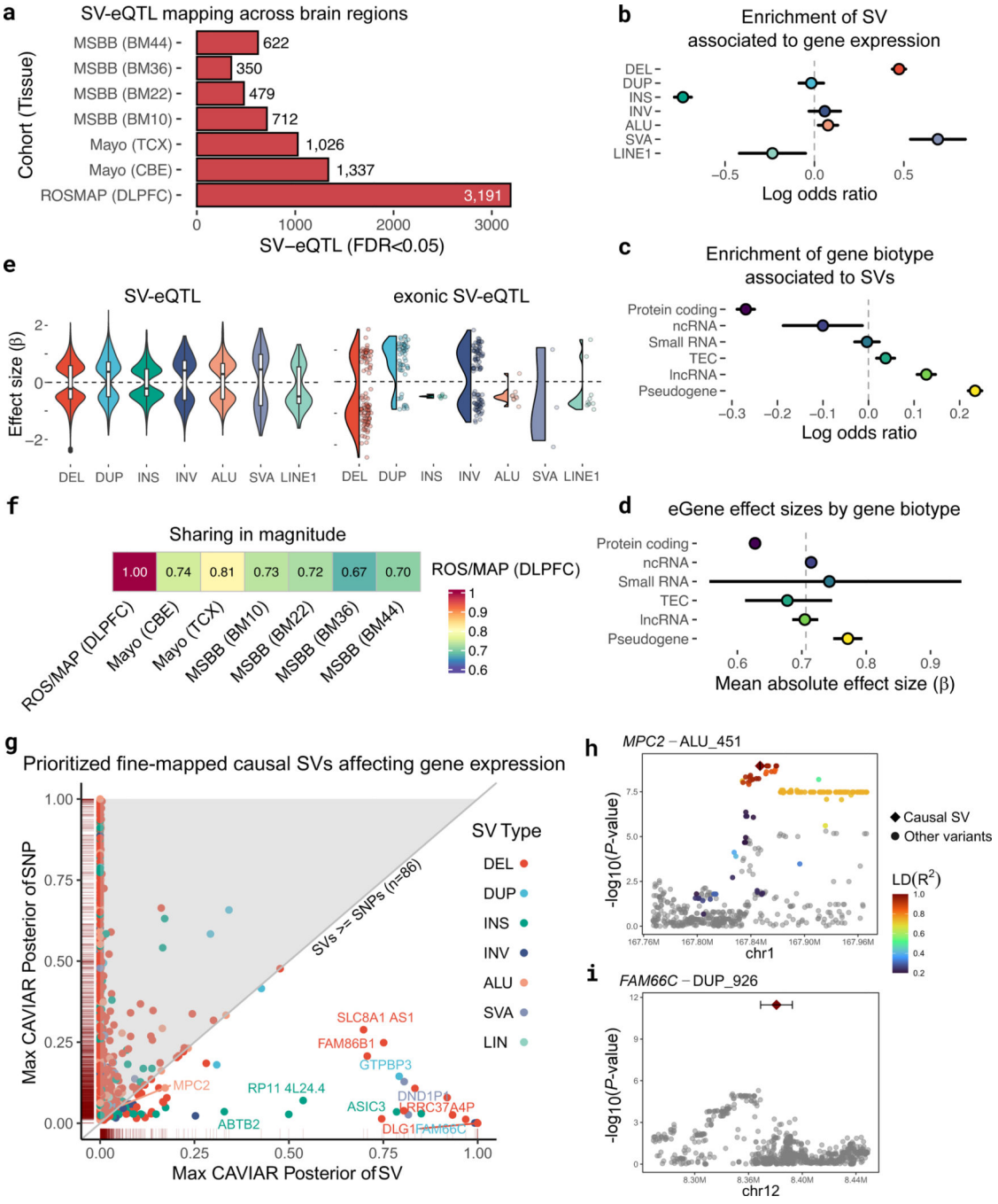

Figure 3 - Properties of SV-eQTLs.

a, Total number of significant SV-eQTLs (FDR < 0.05) identified within each cohort (ROS/MAP, Mayo Clinic, MSBB) in each brain region. **b**, Log odds ratio (midpoints) of SV being associated with gene expression changes (i.e., being an SV-eQTL). Lines indicate 95% Wald confidence intervals. **c**, Log odds ratio (midpoints) of a gene being significantly associated stratified by gene biotype, lines indicate 95% Wald confidence intervals. **d**, Average absolute effect sizes (midpoints) of each eGene stratified by gene biotype, lines represent 95% confidence intervals (n = 1000 bootstraps). **e**, Distribution of effect sizes for each SV type

for all SVs (on the left) and SVs that overlap exonic regions of the associated gene (on the right). For box plots, the median is the central line, the box spans the first to the third quartiles and the whiskers extend 1.5 times the IQR from the box. **f**, SV-eQTL sharing in magnitude according to *mashR* meta-analysis. Values represent the proportion of SV-eQTLs that are in the same direction and within a factor of 2 in size comparing each brain region (columns) to ROS/MAP DLPFC. **g**, CAVIAR posterior probabilities for 2,517 genes with significant SV-eQTL association in ROS/MAP. The x-axis shows the maximum posterior probability for SVs, while the y-axis shows the maximum posterior for SNPs mapped jointly for eQTLs. Variants below the diagonal line have a higher SV posterior than SNP posteriors. Gene names are shown for selected genes. Colors represent the SV type of the best SV associated to each gene. **h-i**, Nominal *P*-values (showed as $-\log_{10}$) for joint-eQTL association tests (linear regression between variant allele and gene expression) for the genes *MPC2* (**h**) and *FAM66C* (**i**) considering both SVs and SNPs. The lead variants are an *Alu* insertion (**h**) and duplication (**i**) both with higher CAVIAR posterior probabilities compared to the best SNPs in the locus. Points are colored by the LD to the lead SV. Error bars over the causal SVs represent their size.

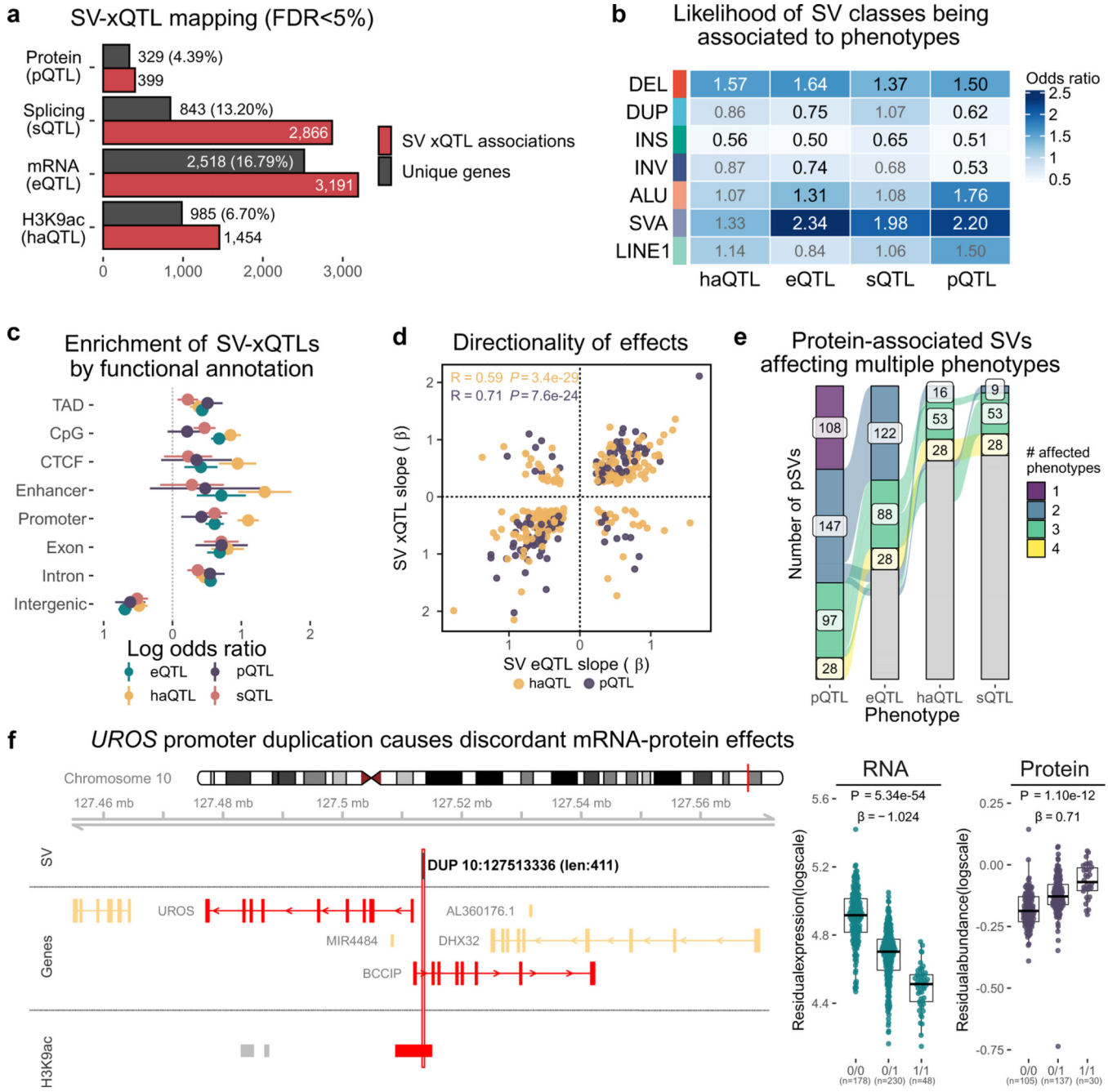

Figure 4 - Impact of SVs on the gene-regulatory cascade.

a, Total number of SV-xQTLs (FDR < 0.05) identified in ROS/MAP. Red bars show the number of lead per phenotype associations measured for each SV class separately, while gray bars show the total number of unique genes associated independently of SV classes. Percentages shown in the gene bars refer to the total number of genes tested for each phenotype. **b**, Heatmap showing the odds ratio of each SV class being associated with changes in each phenotype (i.e., being an SV-xQTL). Odds ratios are measured against all lead SVs per phenotype, including non-significant. Numbers in bold represent *P*-value < 5% (two-sided Wald's test). **c**, Enrichment of xSVs (i.e., SVs significantly associated to some

phenotype) by functional annotation. Values are given as the log odds ratio (midpoints) of an xSV being overlapping a given genomic feature compared to all SVs tested for each molecular phenotype separately. Lines indicate 95% Wald confidence intervals. **d**, Slope correlation of SV-haQTL and SV-pQTL effect sizes (y-axis) compared to SV-eQTL effect sizes (x-axis). Pearson correlations and respective *P*-values (two-sided) are shown for each pair. **e**, SVs associated with proteins (380 pSVs, first bar) that are also associated with different molecular phenotypes (indicated at respective columns). Each color represents pSVs where the same SV-gene pair is significantly associated with a different number of phenotypes, from 1 (only at protein level) to 4 (all molecular phenotypes). **f**, Example of discordant effect between RNA and protein caused by a 411 bp duplication overlapping an H3K9ac peak upstream of the *UROS*. In the locus plot, genes and histone peaks colored in red had significant associations (FDR < 0.05) with the duplication. Box plots show in the y-axis the *UROS* mRNA (n = 456 biologically independent samples) and protein (n = 272 biologically independent samples) residual levels for specific SV allele carriers (x-axis). The box plots show the median in the central line, the box spans the first to the third quartiles and the whiskers extend 1.5 times the IQR from the box. Slopes (β) and FDR adjusted *P*-values are shown for each association (linear regression model).

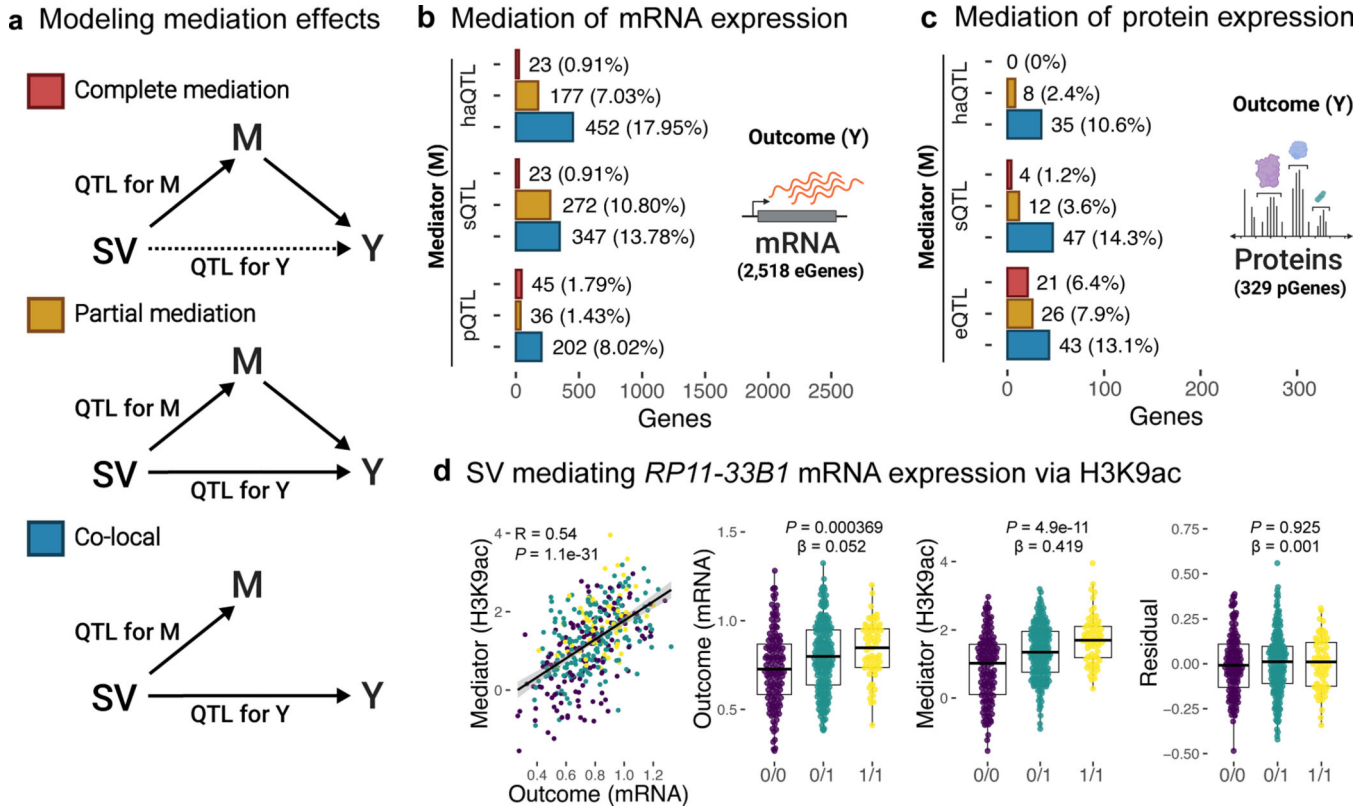

Figure 5 - Mediation of SV-xQTL.

a, Relationships modeled in the mediation testing. The complete mediation model and the partial mediation model represent cases where the effect of an SV on a phenotype Y (also called outcome, e.g. SV-eQTL) is explained, completely or partially, by the effect of the same SV on a phenotype M (also called mediator, e.g. SV-haQTL). The co-local model represents a special case where there is no mediation between M and Y, but the SV independently affects M and Y. **b**, Proportion of 2,518 genes with significant SV-eQTL (mRNA as outcome Y) mediated by either haQTL, sQTL, or pQTLs according to each model. **c**, Proportion of 329 genes with significant SV-pQTLs (proteins as outcome Y) mediated by either haQTL, sQTL, or eQTLs according to each model. **d**, Example of a complete mediation (posterior probability = 0.95) for an SV-eQTL for the gene *RP11–33B1* (outcome) via an SV-haQTL (mediator). The first plot shows the correlation between both phenotypes, x-axis is the residual expression of *RP11–33B1* and the y-axis is the residual values for the corresponding H3K9ac peak (hg19 coordinates 4:120,375,241–120,377,352). The box plots show the associations of an *Alu* insertion (length: 281 bp; hg19 coordinates 4:120,639,905) with the RNA expression, the histone acetylation levels, and the residual expression of *RP11–33B1* after regressing the effects of the histone acetylation levels, respectively (n = 401 biologically independent samples with RNA-seq and H3K9ac data available). The box plots show the median in the central line, the box spans the first to the third quartiles and the whiskers extend 1.5 times the IQR from the box. Slopes (β) and nominal *P*-values are shown for each association (linear regression model).

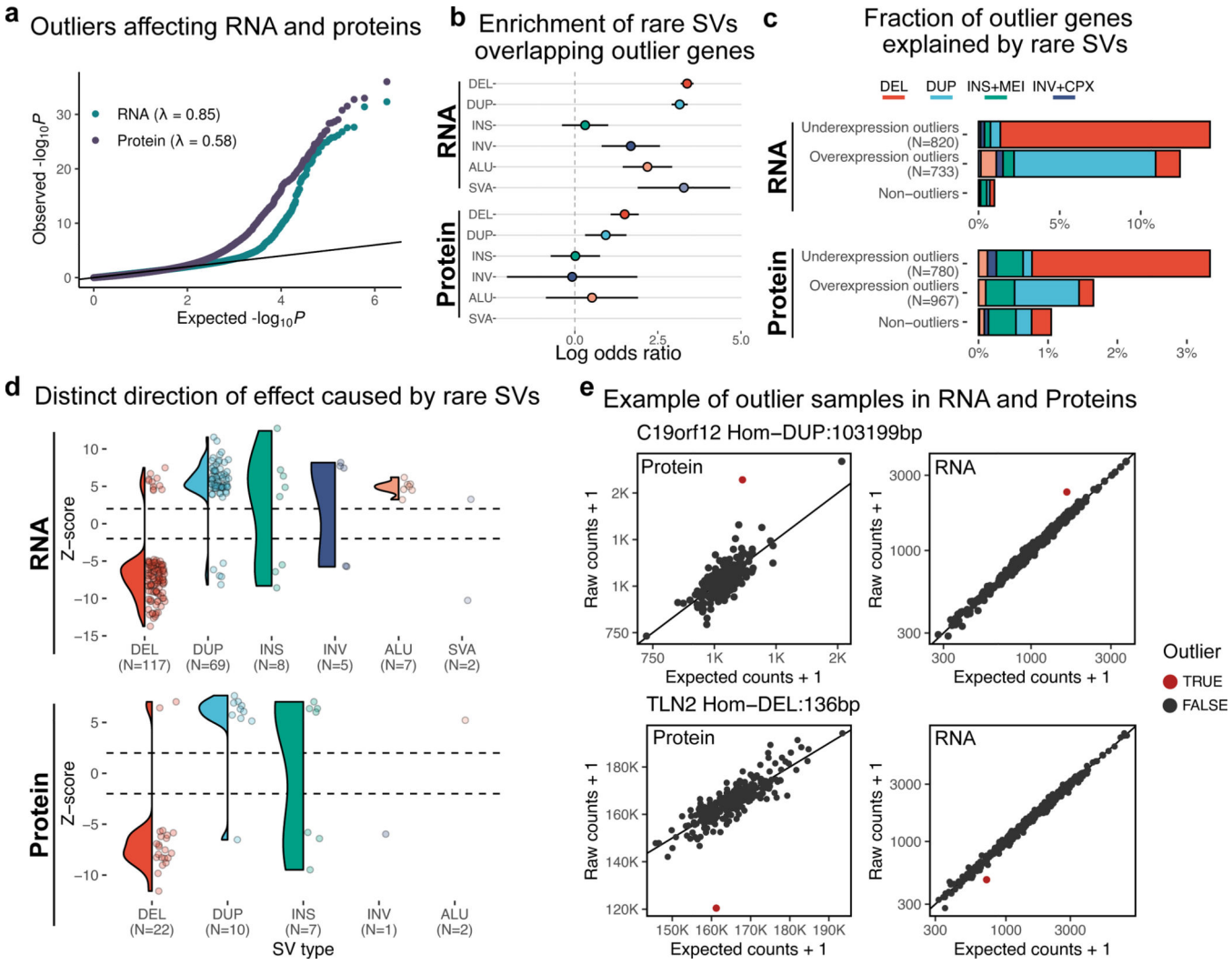

Figure 6 - Impact of rare SVs on gene expression outliers.

a, Quantile-quantile (QQ)-plot showing the observed distribution of *P*-values of outliers for RNA and protein and its deviation from the expected uniform distribution (showing only for gene-sample pairs measured in common). **b**, Enrichment of rare SVs overlapping outliers (any SV breakpoint within the gene body) stratified by SV type showed as a log odds ratio (midpoints) with 95% Wald confidence intervals. **c**, Fraction of overexpressed and underexpressed outlier genes that are potentially explained by each rare SV compared to non-outliers. **d**, Distribution of gene outlier z-scores that are overlapped by rare SVs. **e**, Examples of gene-sample pairs outlier with a rare SV overlapping their respective gene bodies. Showing on top an overexpression outlier for *C19orf12* caused by a 103 kb duplication and at bottom an underexpression outlier for the gene *TLN2* caused by a rare 136 bp deletion. Each dot represents a sample. Y-axis represents the raw counts + 1, while the x-axis represents the expected counts + 1, which is given assuming a negative binomial distribution with a gene-specific dispersion according to the *OUTRIDER'* model. Red dots represent an outlier sample.

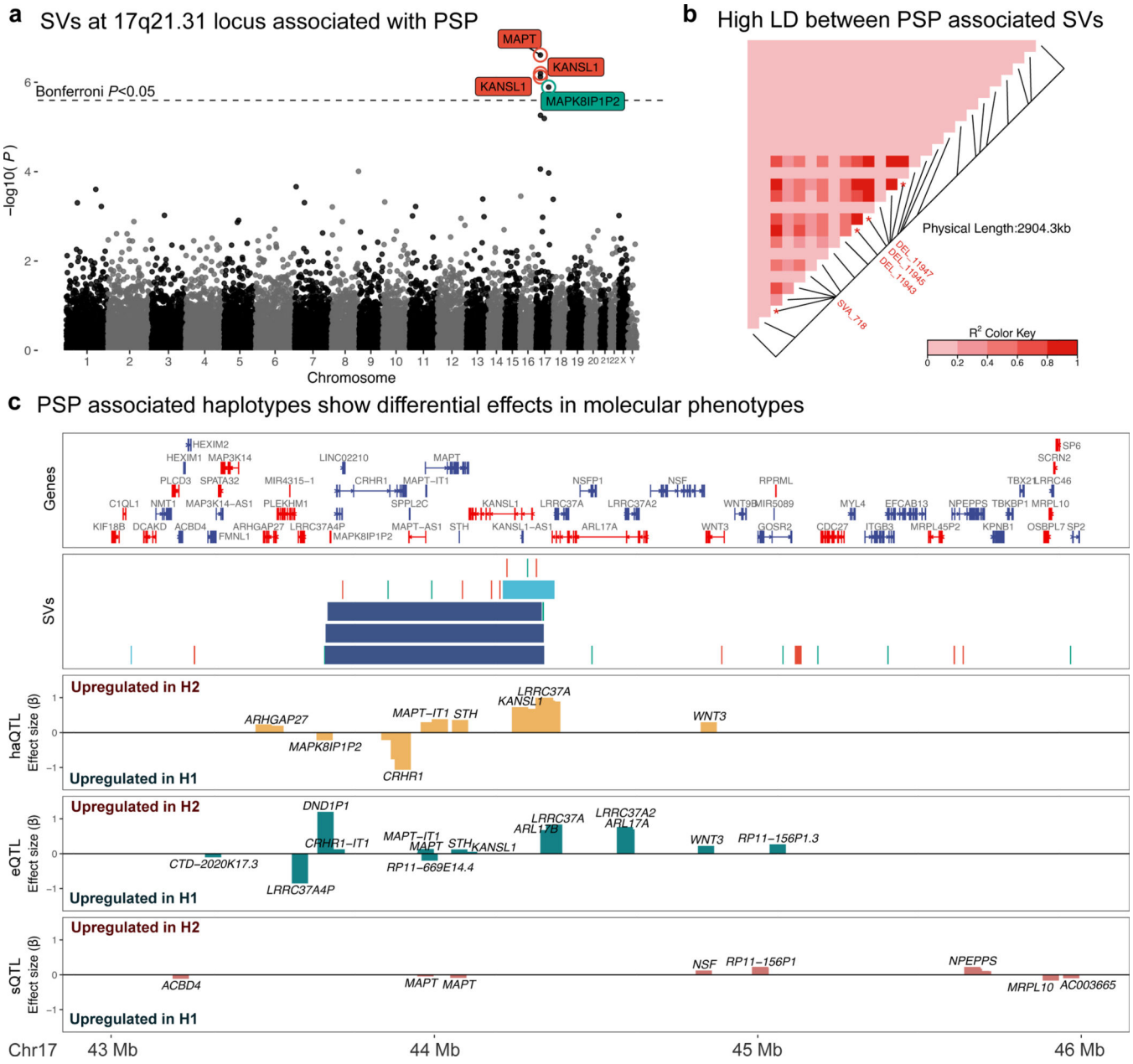

Figure 7 - SVs associated with PSP and their effects on molecular phenotypes.

a, Manhattan plot showing SVs associated with PSP cases (n=83) versus controls (n=368). Estimates were measured using Bayesian logistic regression (bayesglm) accounting for sex, study, and the first three ancestry PCs. Y-axis shows the -$\log_{10}$(*P*-value) of each SV association. X-axis represents SV sequential position by chromosome (not real scale). Labels with names of the nearest gene upstream of each SV breakpoint are shown for SVs with Bonferroni adjusted *P*-values lower than 5% (dashed line). Label colors represent different SV classes. **b**, Pairwise linkage disequilibrium (LD) matrix of SV genotypes identified between chr17:43M-46M (hg19) measured as R^2 (LDheatmap R package). Labels are shown for the SVs significantly associated with PSP status (from letter a). **c**, Locus plot of 17q21.31 locus (chr17:43M-46M (hg19)). Genes bodies are shown at the top track, SVs

with MAF ≥ 1% identified in ROS/MAP are shown at the second track (colors represent SV class), and effect sizes for H1-H2 inversion haplotypes (using the top PSP associated SVs - DEL_11943 - as a proxy) are shown in the remaining tracks. Effect sizes are shown only for significant associations (FDR < 0.05). Positive effect sizes indicate increased levels of each phenotype in individuals with H2 (inverted) haplotype.